

Finite-size Lagrangian coherent structures in thermocapillary liquid bridges

Francesco Romàn*

*Institute of Fluid Mechanics and Heat Transfer, Technische Universität Wien, Getreidemarkt 9,
1060 Vienna, Austria
and Department of Biomedical Engineering, University of Michigan, 2123 Carl A. Gerstacker Building,
2200 Bonisteel Boulevard, Ann Arbor, Michigan 48109-2099, USA*

Hendrik C. Kuhlmann

*Institute of Fluid Mechanics and Heat Transfer, Technische Universität Wien, Getreidemarkt 9,
1060 Vienna, Austria*



(Received 23 October 2017; published 4 September 2018)

The rapid accumulation of small, finite-size rigid particles along closed rotating threads in high-Prandtl-number thermocapillary liquid bridges is investigated numerically when the flow arises as a traveling hydrothermal wave. For a dilute suspension, different motion models are investigated which could provide the dissipation mechanisms leading to the experimentally observed particle-motion attractors. Making use of a phenomenological particle-boundary interaction model, it is shown that the particle size effect, which becomes important when the particle moves near the thermocapillary free surface, provides the relevant source of dissipation for the remarkably fast particle accumulation. Furthermore, the accumulation phenomenon is tightly correlated with the Kolmogorov-Arnold-Moser (KAM) tori of the flow in the absence of particles. Therefore, KAM tori in the rotating frame of reference, in which the flow field is steady, can be considered templates for the accumulation structures. The numerical results obtained are compared with experimental data for the so-called spiral loop 1 and spiral loop 2 particle accumulation structures. In addition, other accumulation structures are numerically predicted which yet await experimental confirmation.

DOI: [10.1103/PhysRevFluids.3.094302](https://doi.org/10.1103/PhysRevFluids.3.094302)

I. INTRODUCTION

Particle-laden flows are characterized by the motion of a dispersed phase of rigid particles in a continuous fluid phase. Such flows are important in many natural phenomena arising on different length scales ranging from nano- and micrometers (e.g., the transport of red blood cells [1]), over macroscopic scales (e.g., in debris flows [2]), up to astronomical scales (e.g., in planetary formation [3]). Furthermore, particle-laden flows play a major role in many industrial applications and in the environment (e.g., in combustion [4], drug delivery [5], and airborne dust [6]). Particle-laden flows can be classified depending on the physical parameters of the particulate and the fluid phase. The behavior is quite distinct, depending on the suspension being dense or dilute, the timescales of the particle and the flow being disparate or similar, and the particles being active or passive. Starting from an initially random and dilute distribution of small passive particles, the initial and intermediate evolution of the system can be treated by neglecting the mutual interaction among particles and the influence of the particles on the fluid flow. This approach is commonly referred to as one-way coupling.

*frromano@umich.edu

In experimental fluid mechanics, small particles are frequently employed to visualize the flow or to measure its velocity. For that purpose, the particles ought to behave like tracers. However, when they are dispersed in a thermocapillary liquid bridge [7], small particles were found to cluster in curious shapes [8] which the authors called *particle accumulation structures* (PAS). Surprisingly, the demixing took place over very short timescales (a few seconds), despite of the small Stokes number of the order of $St = O(10^{-5})$ and a mass density of the particles comparable to that of the carrier fluid.

Over the last two decades, PAS has received increasing attention. PAS can be observed in three-dimensional thermocapillary flows in axisymmetric liquid bridges when the flow arises as an azimuthally traveling hydrothermal wave. The hydrothermal wave emerges from an instability of the steady axisymmetric toroidal vortex flow and its temperature field [9,10]. The properties of PAS and its relation to the underlying traveling hydrothermal wave have been studied by Tanaka *et al.* [11] and Schwabe *et al.* [12]. These authors found that the accumulation structure typically takes the shape of a closed thread of particles which is spirally wrapped around the core of the basic toroidal vortex. The spiral shape of the accumulation structure travels azimuthally with exactly the same angular velocity as the hydrothermal wave, whereas individual particles may even move opposite to the wave in the mean [11], while they primarily circulate like the fluid about the vortex core.

When the hydrothermal wave arises with an azimuthal wave number $m = 3$, the spiralling PAS typically has the same wave number, but it can be three (so-called SL-1 PAS, where SL denotes spiral loop) or six times wound about the vortex core (SL-2 PAS) before closing on itself. Schwabe *et al.* [12] found that the shape of PAS is independent of the particle shape, no matter if spherical or irregular. Moreover, PAS was found to form most quickly if the particles were density matched to the fluid and if the particles have an appreciable size. Particles too small would not form PAS. These observations were the first hints that the particle size was the most important parameter, while inertial effects were of minor importance in their experiments. Since PAS was also observed under conditions of weightlessness [13], albeit for somewhat different flow conditions, buoyancy forces cannot be held responsible for PAS.

Based on the observations of Schwabe *et al.* [12], Hofmann and Kuhlmann [14] suggested a mechanism by which PAS can arise. Accordingly, PAS is an attractor for the motion of *individual* particles, when particle-particle interactions can be neglected during the initial phase of PAS formation. In their model, the centroid of the particles cannot approach the free surface arbitrarily close, due to their finite size. This effect may not be significant in many flows with stationary solid walls, but in thermocapillary flows with a strong streamline crowding toward the free surface [15], it can be important. Moreover, Hofmann and Kuhlmann [14] numerically found that the streamlines of the hydrothermal-wave state consist of regular and chaotic streamlines [16,17]. Assuming perfect advection, they described PAS as the transfer of particles from chaotic streamlines to regular ones by way of collision of the finite-size particles with the free surface. Considering the particle orbits during the collision phase, they suggested PAS arises either as a periodic orbit winding on a KAM torus and closed near the free surface by the particle-surface interaction process, or as a KAM torus on which particles cluster and where the torus depends the particle size. The work of Hofmann and Kuhlmann [14] was continued and confirmed by Mukin and Kuhlmann [18] using a much higher numerical accuracy. Muldoon and Kuhlmann [19] explored the implications of the particle-surface interaction (PSI) model of Hofmann and Kuhlmann [14] using a closed-form model flow which was fitted to a traveling hydrothermal wave. This approach avoids interpolation errors which are unavoidable in discrete simulations and which impair an accurate computation of the streamlines, i.e., the trajectories of advected particles [20].

In the past, characteristic patterns due to the depletion of particles near the axis of the liquid bridge have been utilized to visually identify the azimuthal wave number of the hydrothermal wave. The reason for the particle depletion patterns, however, remained unknown. Muldoon and Kuhlmann [19] have explained these patterns as fingerprints of the particle-surface interaction when the particle size is very small. For subcritical flow, the axial projection of the depletion zone is circular. By fully resolved two-dimensional simulations of the Navier-Stokes equations, without resorting to any

particle-motion model, Romanò and Kuhlmann [21] have shown that the one-parameter collision model of Hofmann and Kuhlmann [14] is indeed a good approximation to the fully resolved particle-surface interaction, if the interaction parameter Δ , i.e., the minimum admissible distance of the particle's centroid from the free surface, is selected correctly. A good PSI model should take into account not only the size of the particle but also the lubrication gap δ between the particle and the free surface [18,21,22], where δ is a function of the flow and particle parameters [21]. Selecting Δ correspondingly, Romanò and Kuhlmann [22] obtained a good agreement between the single-particle motion measured experimentally and the numerical simulation of the particle based on the Maxey-Riley equation [23] and the PSI model. They have shown that particles are attracted, in axisymmetric thermocapillary flow in liquid bridges, to a toroidal surface, as predicted qualitatively [19]. These results provided solid evidence for the existence and significance of the particle-surface interaction, which was also confirmed recently in a microflow with particles as small as 250 nm in radius [24].

In contrast to the explanation of three-dimensional PAS in terms of particle-surface interaction and a specific flow topology, Pushkin *et al.* [25] and Melnikov *et al.* [26] advocated a mechanism which is essentially based on particle inertia and does not rely on the particle-surface interaction. This controversial point of view evoked comments by Kuhlmann and Muldoon [27,28] with corresponding replies [29,30]. As a matter of fact, however, all authors who numerically investigated PAS in thermocapillary liquid bridges have included the PSI model of Hofmann and Kuhlmann [14] in some way or the other, even if not mentioned explicitly [31,32]; see Ref. [33].

In recent years, several investigations have been devoted to establishing the properties of PAS experimentally or numerically. While Kuhlmann *et al.* have focused on simulations for $Pr = 4$ [15,18,21,22,33], Shevtsova *et al.* have considered $Pr = 13$ corresponding to *n*-decane, which was employed as the working fluid in experiments [26,34–36]. Ueno *et al.* have carried out experiments for $Pr = 28$ using silicone oil [11,37–40].

Despite the solid experimental data basis for PAS in liquid bridges of $Pr = 28$, numerical results are lacking. The primary reason is the high grid resolution of the flow required to accurately compute streamlines and trajectories and to resolve the particle-surface interaction. Therefore, we consider the flow topology and the motion of particles in thermocapillary liquid bridges of $Pr = 28$ for selected cases, for which data are available from experiments with silicone oil under normal gravity conditions. It will be shown that PAS is tightly related to the flow topology in the absence of particles, confirming the role of the KAM tori and the closed streamlines for PAS established by Hofmann and Kuhlmann [14] and Mukin and Kuhlmann [18] for $Pr = 4$. Furthermore, it will be proven that the relevant dissipative mechanism for PAS at $Pr = 28$ is the particle-boundary interaction which relies on the finite particle size. Since PAS for $Pr = 28$ is caused by the finite size and not by the inertia of the particles, this result naturally leads to the notion of *finite-size Lagrangian coherent structures*.

In Sec. II, the mathematical formulation of the problem will be presented, addressing the assumptions made to simplify the calculation of the streamline topology and the particle trajectories. Section III describes the numerical methodologies employed for simulating the flow and the particulate phase. In Sec. IV, the results are presented. Simulations are carried out for experimental conditions for which the accumulation of particles is well documented. The finite-size Lagrangian coherent structures computed and validated by experiments are correlated with the flow topology. Finally, in Sec. V, the results are summarized and conclusions are drawn.

II. PROBLEM FORMULATION

A liquid bridge of an incompressible Newtonian liquid with density ρ_f , thermal diffusivity κ , and kinematic viscosity ν is considered. The fluid properties are assumed to be constant. Two coaxial, circular cylindrical rods of radius R are kept at a mutual distance d to support the liquid bridge. The axis of the liquid bridge is oriented parallel to the gravity vector \mathbf{g} and the two rods are differentially heated, keeping the bottom rod at a constant cold temperature $T_{\text{cold}} = T_0$, while the top rod is maintained at a constant hot temperature $T_{\text{hot}} = T_0 + \Delta T$, with ΔT being the temperature difference.

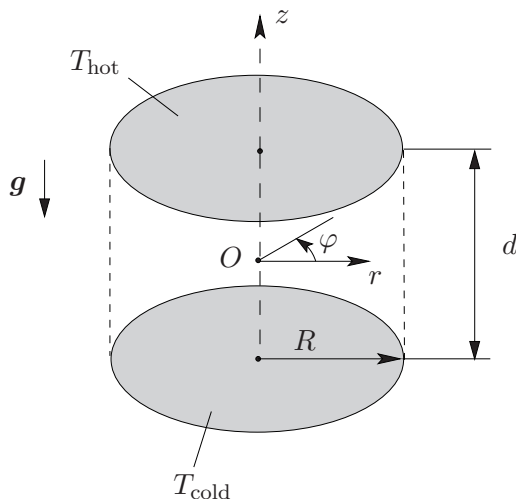


FIG. 1. Geometry of the liquid bridge and coordinate system.

To linear order, the surface tension σ between the liquid and the ambient gas is approximated by

$$\sigma(T) = \sigma_0 - \gamma(T - T_0), \quad (1)$$

where $\sigma_0 = \sigma(T_0)$ and $\gamma = -\partial\sigma/\partial T|_{T=T_0}$ is the negative surface-tension coefficient. We consider an asymptotically large reference surface tension σ_0 such that the capillary pressure dominates and the shape of the interface is independent of the flow field. If we neglect deformations due to gravity forces, a liquid bridge with volume $\mathcal{V} = \pi R^2 d$ takes a cylindrical shape (see Fig. 1), which is a reasonable approximation to typical experiments on the millimeter scale [41,42].

A. Fluid flow

The flow in the liquid bridge is governed by the nondimensional Navier-Stokes, continuity and energy equations which are considered in Oberbeck-Boussinesq approximation

$$(\partial_t + \mathbf{u} \cdot \nabla) \mathbf{u} = -\nabla p + \nabla^2 \mathbf{u} + \text{Gr} \theta \mathbf{e}_z, \quad (2a)$$

$$\nabla \cdot \mathbf{u} = 0, \quad (2b)$$

$$\text{Pr}(\partial_t + \mathbf{u} \cdot \nabla) \theta = \nabla^2 \theta, \quad (2c)$$

where $\mathbf{u} = u\mathbf{e}_r + v\mathbf{e}_\varphi + w\mathbf{e}_z$ is the velocity vector field in cylindrical coordinates (r, φ, z) with origin in the center of the liquid bridge, $\mathbf{x} = r\mathbf{e}_r + z\mathbf{e}_z$ is the position vector with unit vectors $(\mathbf{e}_r, \mathbf{e}_\varphi, \mathbf{e}_z)$, p is the pressure, and t is the time. The governing equations have been made dimensionless using the viscous scaling d , v/d , d^2/ν , and $\rho_f v^2/d^2$ for length, velocity, time and pressure, respectively. The reduced temperature is defined as $\theta = (T - T_0)/\Delta T$. The nondimensional groups arising in (2) are the Prandtl and the Grashof numbers which are defined, respectively, as

$$\text{Pr} = \frac{\nu}{\kappa} \quad \text{and} \quad \text{Gr} = \frac{g\beta\Delta T d^3}{\nu^2}, \quad (3)$$

where β and g are the thermal expansion coefficient and the acceleration of gravity, respectively.

The mathematical problem given by the bulk equations (2) is closed by enforcing no-slip and constant-temperature boundary conditions on the differentially heated rods

$$z = \pm 1/2: \quad u = v = w = 0, \quad \theta = 1, 0. \quad (4a)$$

If we neglect viscous forces of the ambient gas on the liquid-gas interface and modeling the heat transfer across the free surface by Newton's law of cooling, with the ambient gas being at the constant cold-wall reference temperature, the boundary conditions on the free surface can be written as

$$r = 1/\Gamma : \quad \mathbf{u} = 0, \quad \mathbf{e}_r \cdot \mathcal{S} \cdot \mathbf{e}_z = -\text{Re} \partial_z \theta, \quad \mathbf{e}_r \cdot \mathcal{S} \cdot \mathbf{e}_\varphi = -\frac{\text{Re}}{r} \partial_\varphi \theta, \quad \partial_r \theta = \text{Bi} \theta, \quad (4b)$$

where $\mathcal{S} = \nabla \mathbf{u} + (\nabla \mathbf{u})^T$ is the viscous stress tensors in the liquid. From (4b), three additional nondimensional groups arise: the thermocapillary Reynolds number Re , the Biot number Bi , and the aspect ratio Γ , defined as

$$\text{Re} = \frac{\gamma \Delta T d}{\rho_f \nu^2}, \quad \text{Bi} = \frac{hd}{k}, \quad \text{and} \quad \Gamma = \frac{d}{R}, \quad (5)$$

respectively, where h is the heat-transfer coefficient and k is the heat conductivity of the liquid. For comparison with experiments, also the Marangoni number $\text{Ma} = \text{RePr}$ is introduced.

In view of the large number (five) of nondimensional parameters involved and the computational cost of highly resolved numerical simulations, we focus on flow conditions for which experimental results are available. Therefore, we consider $\Gamma = 0.68$, $\text{Pr} = 28$, and select $\text{Bi} = 0.3$. These are parameters for which different particle accumulation structures have been found experimentally ranging from SL-1, SL-2 [11,39], and their combinations to the so-called toroidal core [15,39]. In these experiments, the length scale was $d = 1.7$ mm.

B. Particle motion

Within the one-way coupling approximation used, the fluid flow can be computed independently from the particle motion. To model the motion of a spherical particle in the liquid bridge, we employ the simplified version by Babiano *et al.* [43] of the Maxey-Riley equation [23]

$$\ddot{\mathbf{y}} = \left(\frac{1}{\varrho + 1/2} \right) \left[-\frac{\varrho}{\text{St}} (\dot{\mathbf{y}} - \mathbf{u}) + \frac{3}{2} \frac{D\mathbf{u}}{Dt} - \frac{(\varrho - 1)}{\text{Fr}^2} \mathbf{e}_z \right], \quad (6)$$

where we use the same viscous scaling as for the Oberbeck-Boussinesq equations. The position vector of the particle centroid is denoted \mathbf{y} and D/Dt is the Lagrangian derivative with the flow field. The Basset term, the Saffman and the Faxén corrections are neglected.

Three additional nondimensional groups arise for the particle motion: the particle-to-fluid density ratio ϱ , the Stokes number St , and the Froude number Fr , which are defined, respectively, as

$$\varrho = \frac{\rho_p}{\rho_f}, \quad \text{St} = \varrho \frac{2a_p^2}{9d^2}, \quad \text{and} \quad \text{Fr} = \frac{v}{\sqrt{gd^3}}, \quad (7)$$

where a_p is the radius of the spherical particle and ρ_p is its density.

The one-way coupling approach (6) yields a good approximation to the motion of a particle far away from the boundaries of the domain when the Stokes number $\text{St} \ll 1$ is small, the particle Reynolds number $\text{Re}_p = (a_p/d)|\dot{\mathbf{y}} - \mathbf{u}| \ll 1$ is small and when the suspension is dilute with a volume fraction of solid less than $O(10^{-3})$. All these assumptions hold in the cases of interest for this study, except when the particle moves close to the domain boundaries or when the local volume fraction of particles is too high to neglect particle-particle interactions (i.e., when many particles gather close to each other). The breakdown of (6) is particularly significant near the free surface, because the streamlines are extremely crowded toward the interface. Therefore, the finite size of the particle cannot be ignored very near the free surface.

To take into account the finite particle size, we employ the particle-surface interaction (PSI) model introduced by Hofmann and Kuhlmann [14] and further improved by Romanò and Kuhlmann [21,44] to account for an estimate of the minimum lubrication gap width δ between the particle and the free surface. Within the phenomenological lubrication approach adopted by the PSI model, the particle motion is ruled by (6) until its centroid has approached the free surface up to a minimum allowable

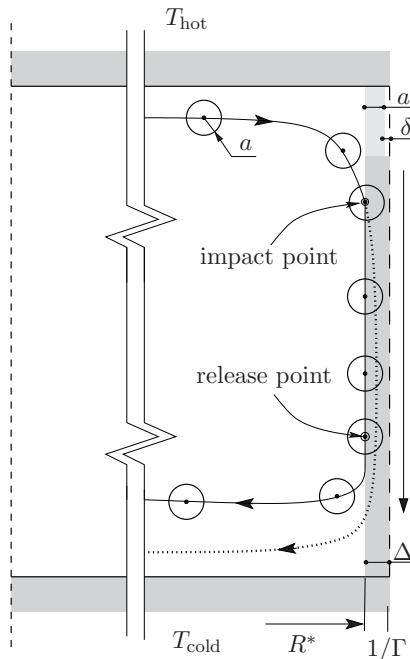


FIG. 2. Sketch of the PSI model for the motion of a spherical particle (circles) with centroid indicated by a dot. The dotted curve represents the particle trajectory in the absence of the PSI model. The full line represents the trajectory when the PSI model is employed. The short-dashed line indicates the axis of the liquid bridge and the long arrow indicates the direction of the thermocapillary stresses along the interface (long-dashed line). The particle radius a , lubrication gap width δ , and interaction parameter Δ are indicated.

distance $\Delta = a + \delta$, comprising the nondimensional particle radius $a = a_p/d$ and a nondimensional characteristic lubrication gap width δ . When a particle approaches the interface from the bulk, the positive radial velocity component \dot{y}_r of the particle is annihilated when it arrives at the distance Δ from the free surface. The remaining velocity components $\dot{y}_\varphi \neq 0$ and $\dot{y}_z \neq 0$ make the particle slide parallel to the free surface until it is transported to a point at which the radial velocity component of the flow field u turns negative. At that point, the particle is released to the bulk and the PSI model ceases. Note that the surface of a perfectly wetted particle approaching a smooth, indeformable free surface (this holds in experiments since $\sigma_0 \gg 1$) cannot make contact with the free surface in a finite time due to the lubrication forces which repel the particle [45]. The existence of a lubrication gap is consistent with experimental observations [22]. A corresponding interaction model is not implemented near the solid walls, because it is irrelevant for PAS in the flows considered, as explained later.

The PSI model is conceptually illustrated in Fig. 2 for a steady axisymmetric flow in a liquid bridge. In considering the lubrication effect between the surface of the completely wetted solid particle and the nondeformable liquid-gas interface, Romanò and Kuhlmann [21] pointed out that the larger and the heavier the particle, the more it is capable of squeezing the lubrication film. On the contrary, for small and lighter (but still $\varrho > 1$) particles, the lubrication gap thickness can become of the same order of magnitude as the particle radius, an effect which cannot be neglected. Therefore, the lubrication gap thickness δ is taken into account using the function $\Delta(a, \varrho)$ proposed by Romanò and Kuhlmann [21], which accounts for drag, lift, and lubrication forces on the particle derived from fully resolved numerical simulations. Specifically, we employ the interpolation

$$\Delta = a \left(1 + \frac{\delta_a}{a}\right) \left(1 + \frac{\delta_\varrho}{a}\right), \quad (8)$$

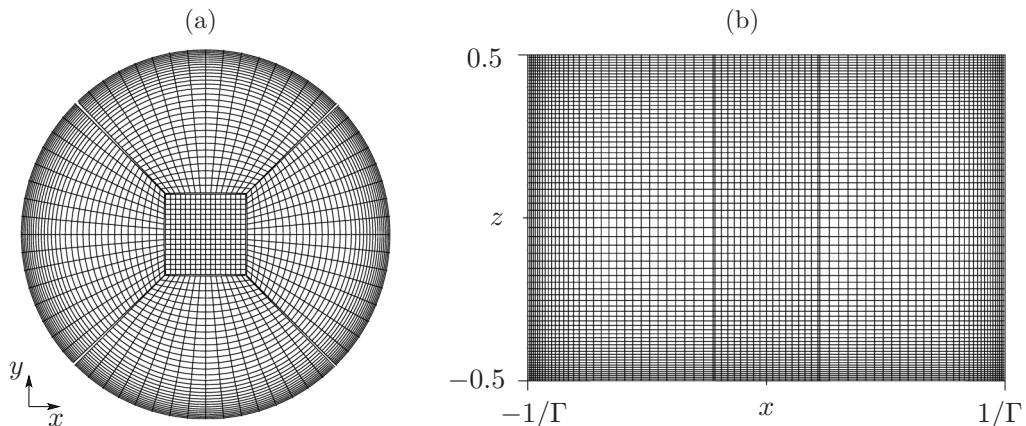


FIG. 3. Distribution of finite volumes in the (x, y) (a) and the (x, z) plane (b). The grid employed for the simulations is five times finer than the one depicted, consisting of ≈ 20 million cells. The double lines indicate the main blocks of the mesher software BLOCKMESH.

where δ_a and δ_o are interpolation functions defined in Refs. [21]. We note the interaction parameter Δ is solely based on fully resolving numerical simulations [21] and does not involve any fit to experimental data. The same approach has been used in Romanò and Kuhlmann [22] and verified by comparison with experimental results for the limit cycle of a single particle moving in the steady axisymmetric flow in a liquid bridge for subcritical conditions.

The PSI model for the particle motion corresponds to an inelastic collision in direction normal to the interface of the particle with the free surface. The model adds significant dissipation to the dynamical system (6), because the kinetic energy of the motion normal to the interface is impulsively dissipated. Therefore, the particle–free-surface interaction can create attractors for the particle motion.

III. NUMERICAL METHODS

A. Fluid flow

A collocated finite-volume solver is employed for the numerical simulations of the fluid flow. The solver has been developed in the framework of the open-source software package OPENFOAM, extending a pressure-based solver to include the thermocapillary stress conditions along the free surface. The details of the numerical implementation of the boundary conditions and a comprehensive code validation can be found in Kuhlmann and Lemée [46].

Figure 3 shows the distribution of the finite volumes which are employed to discretize the domain. All simulations are carried out with a mesh consisting of about 20 million cells. The simulations employ second-order discretization schemes, both in space and time. For the discretization in space, a central scheme is used. Time is advanced implicitly (backward in OPENFOAM). We employ the pressure-implicit with splitting of operators (PISO) algorithm with two external correction steps (`nCorrectors=2`), accounting for the nonorthogonality of the grid via two internal correction loops (`nNonOrthogonalCorrectors=2`). Preconditioned conjugate gradients are used for solving the linear algebraic equation resulting from the pressure-projection step, whereas preconditioned biconjugate gradients are used for the momentum and energy equations. The iterative methods employed for solving these linear systems are terminated when the relative residuals are smaller than 10^{-7} .

To obtain the traveling-wave solution for the selected parameters, a continuation method has been employed using as initial condition the traveling wave obtained by Mukin and Kuhlmann [18] for

$Pr = 4$ and $Bi = 0$ and stepwise increasing the Prandtl and Biot numbers to $Pr = 28$ and $Bi = 0.3$. For each set of fixed parameters (Pr , Bi) the integration in time is carried out using a time-step size of $\Delta t = 1.4 \times 10^{-4}$ until a fully developed hydrothermal wave is established. To ensure convergence, the velocity components and the temperature have been monitored in 16 points distributed in the domain. When the hydrothermal wave with angular velocity Ω is fully developed, the signal at each point will be periodic in time and the flow field is steady in the frame of reference rotating with Ω . To establish a convergence criterion, the flow field is transformed into a frame of reference rotating with $\Omega' = (2\pi/m)f$, where m is the fundamental azimuthal wave number of the flow and f the current peak-to-peak frequency. The simulations are terminated when the convergence criterion

$$\max_{x,i} \frac{|u_i(\mathbf{x}, t) - u_i(\mathbf{x}, t - \Delta t)|}{Re\Delta t} \leq 3 \times 10^{-4} \quad (9)$$

is satisfied in the frame of reference rotating with Ω' , where \mathbf{x} denotes all grid points and i enumerates the Cartesian components of \mathbf{u} . This condition can only be fulfilled if Ω' has become nearly stationary. Once convergence is reached, the corresponding frequency is identified as the frequency of the traveling wave, $\Omega = \Omega'$.

B. Streamlines and particle trajectories

A fully developed hydrothermal wave is steady in the reference frame rotating with the angular velocity Ω of the wave. Taking advantage of this property, the velocity field in the laboratory frame $\mathbf{u}(\mathbf{x}, t)$ is transformed to obtain the velocity $\mathbf{U}(\mathbf{x}) = \mathbf{u}(\mathbf{x}, t_0) - r\Omega\mathbf{e}_\varphi$ in the frame of reference rotating with the azimuthally traveling wave, where $\mathbf{u}(\mathbf{x}, t_0)$ can be any snapshot of \mathbf{u} at time t_0 .

A Lagrangian approach is used for calculating the motion of infinitesimal fluid elements. The position $\mathbf{X}(t)$ of a fluid element moving along the steady streamline in the rotating frame is governed by the advection equation

$$\frac{d\mathbf{X}}{dt} = \mathbf{U}[\mathbf{X}(t)], \quad (10)$$

with initial condition $\mathbf{X}(t = 0) = \mathbf{X}_0$. Equation (10) is solved using the Runge-Kutta Dormand-Prince method [47]. The results obtained by the standard fourth- and fifth-order Runge-Kutta schemes are used to estimate the integration error at each time step. The algorithm is then adapting the time step Δt to make sure the absolute and relative numerical errors are always less than 10^{-7} . Since the flow field is computed in an Eulerian reference frame, it is necessary to interpolate the discrete flow field data \mathbf{U} at the location of the fluid element \mathbf{X} . To that end, \mathbf{U} is interpolated quadratically on each finite-volume cell, consistent with the order of accuracy of the finite-volume solver.

The same numerical method is used for calculating particle trajectories. However, (10) is replaced by the Maxey-Riley equation in the rotating frame of reference [14]

$$\begin{aligned} \ddot{\mathbf{X}} = & \frac{1}{\varrho + 1/2} \left[-\frac{\varrho}{St} (\dot{\mathbf{X}} - \mathbf{U}) + \frac{3}{2} \mathbf{U} \cdot \nabla \mathbf{U} - \frac{(\varrho - 1)}{Fr^2} \mathbf{e}_z \right] - 2\boldsymbol{\Omega} \times \left(\dot{\mathbf{X}} - \frac{3}{2\varrho + 1} \mathbf{U} \right) \\ & - \boldsymbol{\Omega} \times (\boldsymbol{\Omega} \times \mathbf{X}) \left(1 - \frac{3}{2\varrho + 1} \right). \end{aligned} \quad (11)$$

The equation is solved using velocity-matching initial conditions, $\mathbf{X}(t = 0) = \mathbf{X}_0$ and $\dot{\mathbf{X}}(t = 0) = \mathbf{U}(\mathbf{X})$.

IV. RESULTS

A. General structure of the flow field

When the Reynolds number is increased for large Prandtl number, the basic toroidal vortex flow becomes unstable via a forward Hopf bifurcation to a traveling wave [9,10,41,48]. For the aspect

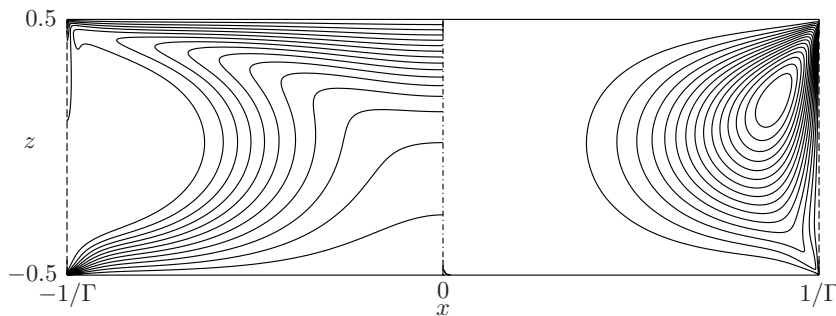


FIG. 4. Isotherms (left) and streamlines (right) of the unstable axisymmetric basic flow for $\Gamma = 0.68$, $Re = 1600$, $Pr = 28$, $Bi = 0.3$, and $Gr = 687$. The dashed lines and the dash-dotted line indicate the free surface and the axis of the liquid bridge, respectively.

ratio $\Gamma = 0.68$ considered, the critical Marangoni number is about $Ma_c \approx 10^4$ [41,49] corresponding to $Re_c \approx 360$ and the critical azimuthal wave number is $m = 3$.

Figure 4 shows the streamlines and isotherms of the unstable basic state at $Re = 1600 \approx 4 \times Re_c$. The strong convective effect at such a large Marangoni number leads to thermal boundary layers on the hot and the cold walls which are particularly thin near the contact lines. The associated large thermocapillary stresses cause a very high surface velocity near the hot wall which is visible by the strong crowding of streamlines near the liquid-gas interface. The streamline crowding is inherited by the three-dimensional flow which can be decomposed into the unstable axisymmetric flow plus a hydrothermal wave with constant amplitude. Since the Grashof number is relatively small, the flow is dominated by the thermocapillary driving as observed in experiments using millimetric liquid bridges (see, e.g., Ref. [39]). This flow feature has important implications for the particle motion and accumulation, because suspended particles can be expected to be frequently transported close to the free surface in the vicinity of the hot wall due to the high volume flux associated with the streamline crowding.

To illustrate the fully developed total flow for $Re = 1600$ for which a hydrothermal wave travels azimuthally along the basic toroidal vortex, the three-dimensional temperature isosurface $\theta = 0.5$ for $Re = 1600$ is shown in Fig. 5(a). It separates cold fluid near the bottom wall from hot fluid near the top wall. The flow field of the hydrothermal wave together with the strong toroidal basic vortex at such a large Marangoni number causes the transport of cold fluid in form of $m = 3$ cold filaments to wrap about the vortex core (not shown) near the hot corner. The first approach of the cold fingers to the free surface are associated with the well-known cold surface spots [12,39]. Since the cold fingers become weaker upon their second return to the free surface, they do not create pronounced secondary cold spots on the free surface. The transport property of the flow field leading to the finger structure of the temperature field is expected to lead to similar structures of transported quantities which are dominated by advection like, e.g., suspended particles.

For the high Reynolds number considered, the spatial spectrum of the hydrothermal wave exhibits the typical harmonics of the fundamental azimuthal wave number $m = 3$. However, we also find very small amplitudes of spectral components with other wave numbers including $m = 1$. The maximum (with respect to r and z) amplitude of the vertical velocity field w with $m = 1$ is only about 0.01% of the maximum amplitude of the fundamental mode with $m = 3$. Since these perturbations do not necessarily have the same azimuthal phase velocity as the dominant mode with $m = 3$ and its harmonics, the hydrothermal wave is almost periodic with $m = 3$, but not exactly. The degree of perturbation of the *perfect* traveling wave can be estimated from Fig. 5(b). The small perturbations found could be due to long transients of decaying spectral components from the initial conditions which also involved grid refinements, or due to physical effects like an instability of the traveling wave [50].

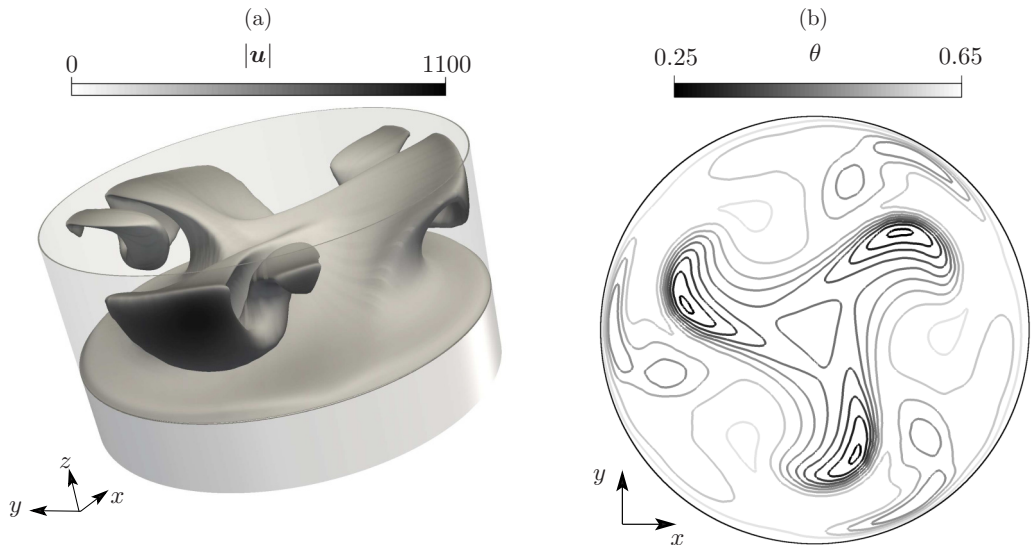


FIG. 5. Temperature field for $\Gamma = 0.68$, $\text{Re} = 1600$, $\text{Pr} = 28$, $\text{Bi} = 0.3$, and $\text{Gr} = 687$. (a) Isosurface $\theta = 0.5$. (b) Isotherms in the midplane $z = 0$. The direction of rotation is clockwise in panels (a) and (b). The gray scale indicates the velocity magnitude in panel (a) and the temperature field in panel (b).

For a deeper understanding of the transport due to the basic flow and the hydrothermal wave, the flow field is analyzed in the rotating frame of reference with respect to the key topological features. Four supercritical Reynolds numbers are considered. The parameter sets are provided in Table I. All sets correspond to experiments of Ueno [51] for which images of experimental particle accumulation structures can be found in Kuhlmann and Lemée [46], except for $\text{Re} = 1750$. In addition, the numerically determined rotation rates Ω of the hydrothermal waves are compared with the values obtained by linear interpolation of the experimental data $\Omega_{\text{exp}}(\text{Ma} = 47000) = 4.30$ and $\Omega_{\text{exp}}(58000) = 4.46$ of Toyama *et al.* [39]. The agreement is very good.

For all cases considered, we find the fully developed supercritical flow to be organized around three fixed points and three limit cycles. These invariant topological elements in the rotating frame are sketched in Fig. 6. The figure also sketches the stable and unstable manifolds of the fixed points and limit cycles. The singular points on the cold and hot walls, denoted s_1 and s_2 , respectively, are degenerate, since the wall-normal flow field in their vicinity vanishes in linear order. They are degenerate spiralling-out saddle foci whose unstable manifolds are on the respective solid wall. Up to computational accuracy, they are located exactly on the axis of symmetry. The limit cycles w_1 and w_2 at the contact lines in the cold and the hot corner, as well as the line of flow separation w_c on the cold wall, are saddle limit cycles and likewise degenerate. Since the unstable manifolds of the saddle foci s_1 and s_2 are located on a solid boundary, the heteroclinic connection of s_1 and s_2

TABLE I. Parameter sets investigated for $\text{Pr} = 28$, $\text{Bi} = 0.3$, and $\Gamma = 0.68$. In addition, the angular velocity Ω of the hydrothermal wave is given and compared with the experimental one Ω_{exp} .

Re	Ma	Gr	Ω	$ \Omega_{\text{exp}} $
1600	44800	687	-4.15	4.27
1750	49000	751	-4.30	4.33
1850	51800	794	-4.36	4.37
1950	54600	837	-4.40	4.41

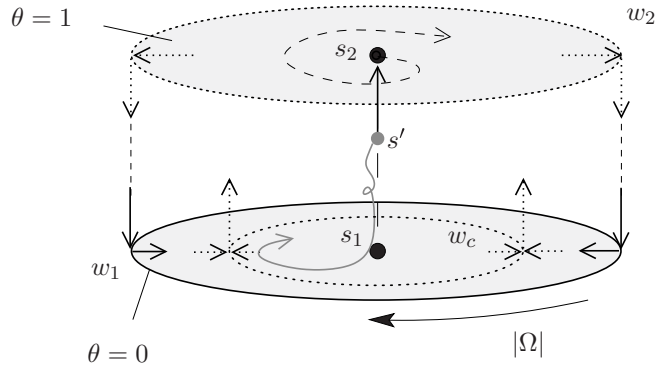


FIG. 6. Sketch of the topological elements of the supercritical flow. The three critical points s_1 , s_2 and s' are indicated by dots. The three limit cycles w_1 , w_2 , and w_c are represented as dotted and full lines. Arrows show the flow along the stable and unstable manifolds. The gray arrow indicates the broken connection between s' and s_1 .

with the saddle limit cycles w_c and w_2 , respectively, must be understood in a degenerate sense. The third singular point s' is a free spiralling-in saddle focus located in close proximity of the z axis ($r_{s'} < 1\%$). Within the given numerical accuracy, s' is heteroclinically connected with s_2 on the hot wall, but disconnected from s_1 on the cold wall, which is shown in Fig. 7(a).

The two saddle limit cycles located in the cold and hot corners w_1 and w_2 are heteroclinically connected with each other along the cylindrical liquid-gas interface. While the stable manifold of w_2 is connected with the saddle focus s_2 , the unstable manifold of w_1 is connected to the saddle limit cycle w_c on the cold wall [Figs. 6 and 7(b)]. Along w_c , the flow separates from the cold wall via

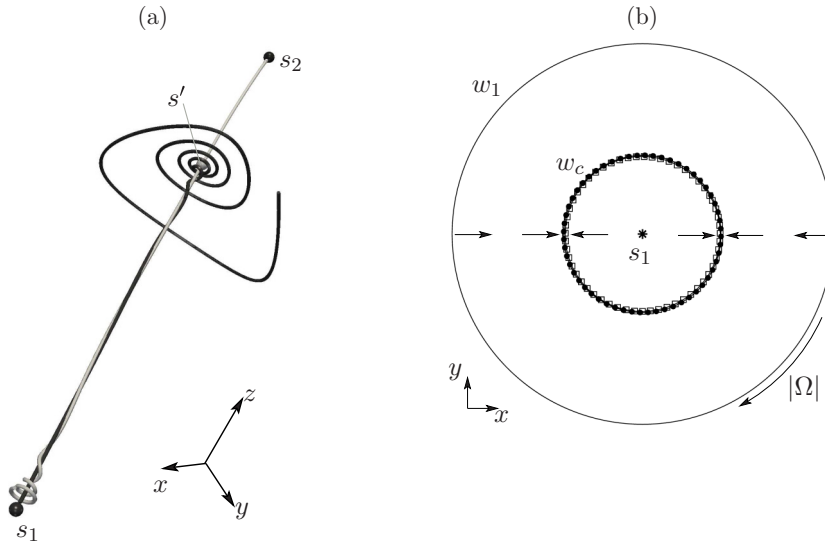


FIG. 7. (a) The broken connection between s_1 and s' for $\text{Re} = 1600$: The two unstable one-dimensional manifolds of s' obtained by integration forward in time are shown in gray. The stable manifold of s_1 (black) obtained by integrating backward in time from s_1 does not connect with s' , but locally approximates the stable manifold of s' . (b) Limit cycle w_c (separation line) on the cold wall for $\text{Re} = 1600$ (dots) and $\text{Re} = 1850$ (squares). The arrows indicate the attraction to w_c (repulsion from w_1) along the cold wall.

a stream surface into the bulk. The line of separation shown in Fig. 7(b) is nearly circular, despite the nonaxisymmetric flow, and nearly independent of the Reynolds number. By comparison with Fig. 4, this separation is not inherited from the axisymmetric basic flow and must therefore be due to the nonlinear interactions among harmonics of the hydrothermal wave which give rise to an $m = 0$ component in the spectrum of the wave. The separation from the bottom wall seems to promote the settling of heavy particles at the bottom of the liquid bridge within the recirculation zone as observed in experiments (see, e.g., Refs. [39,40]).

The broken connection together with the feedback mechanism provided by the axisymmetric part of the flow suggests that at least part of the streamlines are chaotic. The coexistence of regular and chaotic streamlines in a thermocapillary liquid bridge with $\text{Pr} = 4$ has been demonstrated in Ref. [18]. Chaotic and regular flow regions have also been discovered by Refs. [52] and [53] for topologically similar systems.

B. KAM tori and chaotic sea

The fully developed hydrothermal wave is stationary in the rotating frame of reference in the sense of the convergence criterion (9). The small residual perturbation with $m = 1$ has an amplitude which is about 10^4 times smaller than the maximum amplitude of $|U|$ and is thus considered negligible. The incompressible frozen flow in the rotating frame is equivalent to the flux in phase space of a Hamiltonian system with one and a half degrees of freedom [54]. Therefore, regular and chaotic streamlines can coexist in this steady three-dimensional incompressible flow [17,55]. Owing to their relevance for PAS [14,18,19], the analysis of the streamline topology is focused to the regular streamlines inside of Kolmogorov-Arnold-Moser (KAM) tori in the rotating frame of reference.

Regular and chaotic streamlines are indeed found to coexist in the thermocapillary liquid bridge for all cases considered. An initial set of 100 streamlines is reconstructed by initializing fluid elements along four lines near the free surface and parallel to the z axis of the liquid bridge. On each of the lines at $(r, \varphi) = (1/\Gamma - 10^{-3}, n\pi/2)$, $n \in [0, 1, 2, 3]$, 25 fluid elements are initially evenly distributed within $z \in [-0.4, 0.4]$. The streamlines are integrated forward in time up to $t = 30$. The resulting streamlines are then classified as regular or chaotic depending on their ordered returns to the Poincaré plane, selected as $z = 0$. Once regular regions have been identified, corresponding KAM tori are computed with higher accuracy, setting the absolute and relative tolerances of the Dormand-Prince method to 10^{-9} and constraining the maximum time step to $\Delta t_{\max} = 10^{-3}$. The periodic orbits (closed streamlines) in the center of each set of nested KAM tori are determined by computing the elliptic fixed points (Table II) in the Poincaré plane with absolute accuracy of 10^{-3} in the (r, φ) plane using a Newton-Raphson method. Once the closed streamline is obtained, the largest reconstructible KAM torus is obtained from the outermost regular streamline found. This is accomplished considering 200 evenly distributed collocation points along the closed streamline and defining 200 Poincaré planes normal to the closed streamline in these collocation points. The Poincaré points made by the outermost regular streamline are then interpolated, in each Poincaré plane, by cubic splines. From the 200 closed interpolation curves, the *largest* KAM torus is then constructed by cubic Hermitian interpolation.

Figure 8 shows Poincaré sections at midplane $z = 0$ for all four Reynolds numbers considered. Poincaré points of chaotic streamlines are shown in light gray, while Poincaré points of regular streamlines are indicated by black dots. The projection of the largest reconstructible KAM torus is shown as gray shading. Each KAM torus is housing a periodic orbit (full line). To distinguish the different types of KAM tori, we extend the classification proposed by Muldoon and Kuhlmann [19] and name a KAM torus and the associated closed streamline ${}^k T_i^j$ and ${}^k L_i^j$, respectively, where i denotes the azimuthal wave number of the structure and j and k the winding numbers about the basic-flow vortex core and the z axis, respectively, where the winding number is the number of revolutions until the structure closes on itself.

Four topologically different KAM tori are found. For Reynolds numbers $\text{Re} \leq 1850$, we always find a single KAM torus ${}^1 T_3^3$ with wave number $i = m = 3$ which winds $j = 3$ times about the

TABLE II. Characteristic data for the closed streamlines L and the largest reconstructible KAM tori T for different Reynolds numbers. Given are the orbit time τ along the closed streamline in the rotating frame and the minimum distances Δ_{fs} and Δ_w from the free surface and the hot wall, respectively. To define the location of the closed streamline, one of its fixed points in the Poincaré plane $z = 0$ is specified together with azimuthal angle $\varphi_{\theta_{\max}}$ at which the free-surface temperature $\theta_{fs}(\varphi, z)$ reaches a global maximum (hot surface spot).

Re	KAM/streamline	τ	Δ_{fs}	Δ_w	Fixed point (r, φ)	$\varphi_{\theta_{\max}}$
1600	${}^1T_3^3$		0.00565	0.03159		
	${}^1L_3^3$	0.821	0.01180	0.04193	(1.4481, 1.7481)	1.6886
	${}^5T_3^{15}$		0.00562	0.02071		
	${}^5L_3^{15}$	4.2728	0.00582	0.02078	(0.6334, 4.1496)	1.6886
1750	${}^1T_3^3$		0.00851	0.03155		
	${}^1L_3^3$	0.779	0.01462	0.05101	(0.5331, 3.2479)	1.7526
1850	${}^1T_3^3$		0.01041	0.03581		
	${}^1L_3^3$	0.681	0.01251	0.05631	(1.4474, 5.2607)	0.4065
	${}^1T_3^6$		0.00420	0.01467		
	${}^1L_3^6$	1.491	0.00422	0.01470	(0.7073, 0.1757)	0.4065
1950	${}^1T_3^6$		0.00452	0.02070		
	${}^1L_3^6$	1.328	0.00455	0.02072	(1.2050, 3.8304)	0.2596

basic vortex core and once ($k = 1$) about the z axis. For $\text{Re} = 1600$, an azimuthally subharmonic KAM torus ${}^5T_3^{15}$ is found in addition (shown later) which winds 15 times about the vortex core and 5 times about the axis. For $\text{Re} \geq 1850$, another KAM torus ${}^1T_3^6$ is detected, which still has wave number $i = m = 3$, but which winds six times about the vortex core. The cross section of the largest reconstructible KAM surface of ${}^1T_3^6$ is always very small such that the projection of ${}^1T_3^6$ onto the plane $z = 0$ appears smaller than the markers used in Fig. 8. We find the cross section of ${}^1T_3^6$ is growing with Reynolds number such that ${}^1T_3^6$ is slightly larger for $\text{Re} = 1950$ than for $\text{Re} = 1850$. The fourth kind of KAM torus, ${}^0T_3^1$, is only found for the highest Reynolds number, $\text{Re} = 1950$. It is a structure which has an azimuthal wave number $i = 3$. The leading superscript 0 indicates that this torus does not wind about the z axis, unlike, e.g., the tori ${}^1T_1^3$ of Muldoon and Kuhlmann [19].

A three-dimensional view of the reconstructed KAM tori is presented in Fig. 9. It is remarkable that the shape and width of the regular regions do not depend much on the Reynolds number in a wide range of Re but suddenly appear or disappear within the relatively small range. We find all KAM tori of type ${}^1T_3^3$, ${}^1T_3^6$, and ${}^5T_3^{15}$ to pass very close by the free surface of the liquid bridge, while the closest approach to the walls is about three to six times larger and always occurs with respect to the hot wall. Since these geometric parameters are key for explaining the experimentally reported accumulation of particles, the minimum distances between the outermost KAM surfaces and the boundaries are provided in Table II, denoted Δ_w and Δ_{fs} , where the subscripts w and fs refer to the hot wall and the free surface, respectively. Also given are the distances from the boundaries of the closed streamlines and their orbit times τ .

C. Lagrangian finite-size coherent structures

The KAM tori analyzed above are properties of the flow field alone. The fluid inside of KAM tori is locked and does not mix with the fluid outside of the KAM tori. Their importance for particle accumulation has been explained by Hofmann and Kuhlmann [14], who described how particles moving in the region of chaotic streamlines can be transferred to the region of the KAM tori by way of the particle-surface interaction caused by, and depending on, the finite size of the particles. Once moving in the region of the KAM tori of the flow field, the particles are typically prevented to leave this region by repeated collisions with the interface if the deviation of the particle trajectories

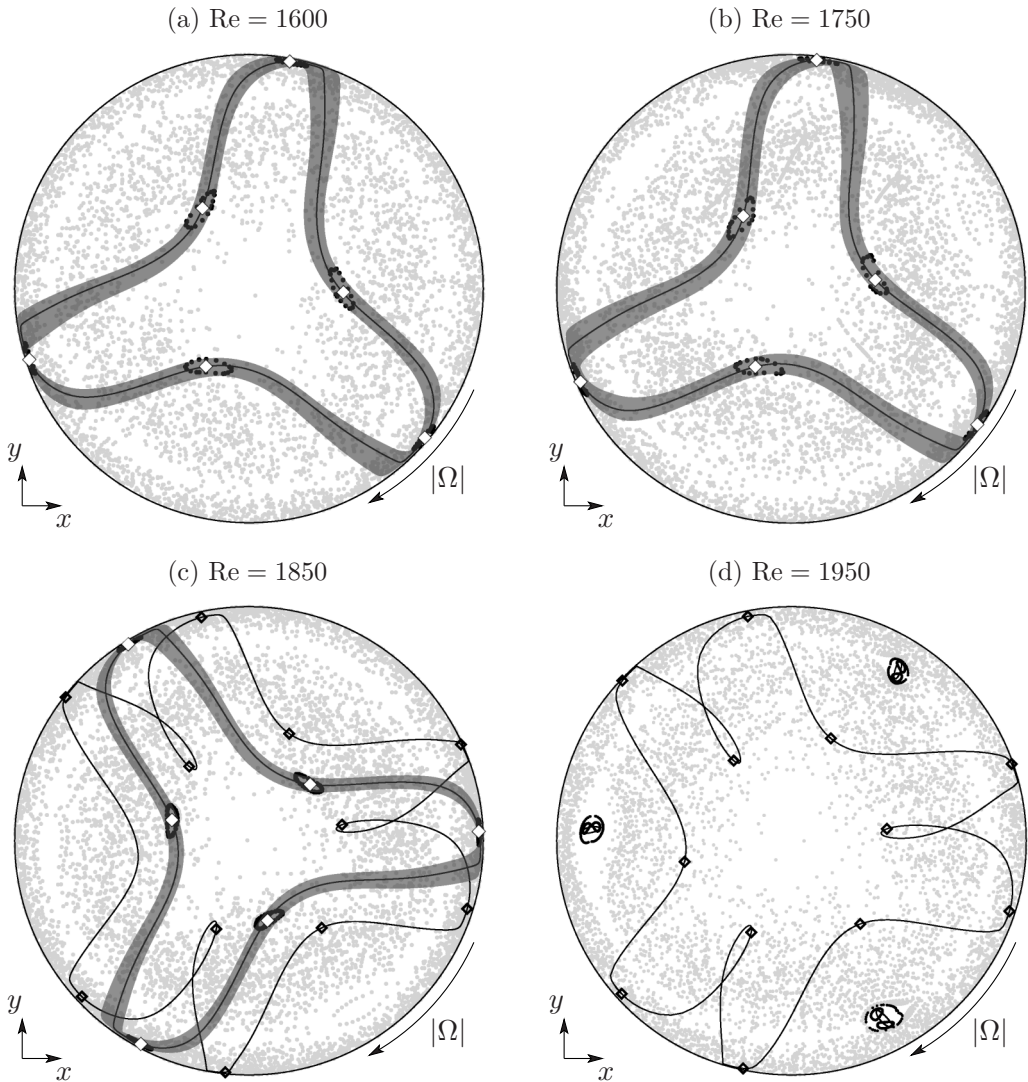


FIG. 8. Poincaré section on the midplane $z = 0$ of chaotic streamlines (light gray dots) and of streamlines on the largest reconstructible KAM tori (black dots) in the rotating frame for (a) $\text{Re} = 1600$ with ${}^1T_3^3$, (b) $\text{Re} = 1750$ with ${}^1T_3^3$, (c) $\text{Re} = 1850$ with ${}^1T_3^3$ and ${}^1T_3^6$, and (d) $\text{Re} = 1950$ with ${}^1T_3^6$ and ${}^0T_3^1$. Also shown are projections of the closed streamlines (lines) and of the largest reconstructible KAM tori (dark gray shading). The intersections of the closed streamlines with the Poincaré plane are marked by diamonds (\diamond). The arrow shows the direction of propagation of the hydrothermal wave in the laboratory frame. Fluid elements in the rotating frame move counterclockwise about the axis in the mean.

from the streamlines is sufficiently small. Exceptions are discussed in Mukin and Kuhlmann [18]. In this respect, the KAM tori are templates for particle motion attractors and the resulting PAS is a *finite-size Lagrangian coherent structure* in contrast to an *inertial Lagrangian coherent structure* which is caused by particle inertia.

To verify this mechanism in liquid bridges of $\text{Pr} = 28$, we consider the motion of finite-size rigid spherical particles in the flow fields studied above using the one-way coupling approach, including

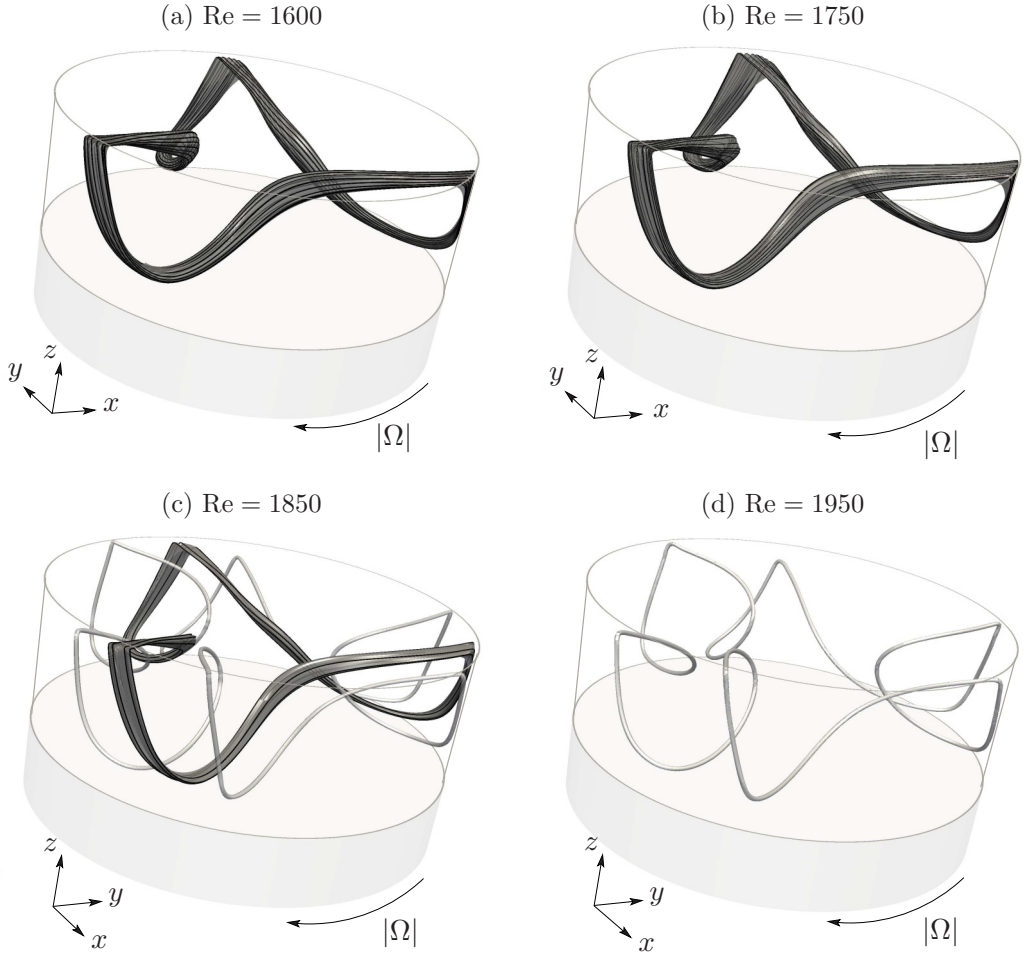


FIG. 9. Three-dimensional view of the largest reconstructible KAM tori ${}^1T_3^3$ (dark gray) and ${}^1T_3^6$ (light gray) for different Reynolds numbers in the rotating frame of reference. A black line on a dark gray KAM torus represents part of the open streamline defining the torus. The arrow shows the direction of propagation of the hydrothermal wave.

drag, lift, buoyancy, and lubrication forces due to particle–free-surface interactions, as described in Sec. II B. Interactions of particles with the solid walls are not taken into account, because these interactions are less frequent and extremely rare or even completely absent during the final stage of the evolution of the particle accumulation process. As will become clear later, the reason is the much closer approach to the free surface of the closed streamlines and the KAM tori as compared to the solid walls (cf. Table II).

The rapid accumulation of particles is a well-established result from experiments for three of the four Reynolds numbers considered [11,38–40]. However, understanding the origin of these accumulation structures is challenging, since different dissipation effects could be responsible for the creation of attractors for the particle motion [14,25,26,31]. While Muldoon and Kuhlmann [33] have shown that particle-surface interaction is the primary cause for PAS for $Pr = 4$ when typical particle parameters are considered, such clear numerical evidence is not available for fluids with $Pr = 28$.

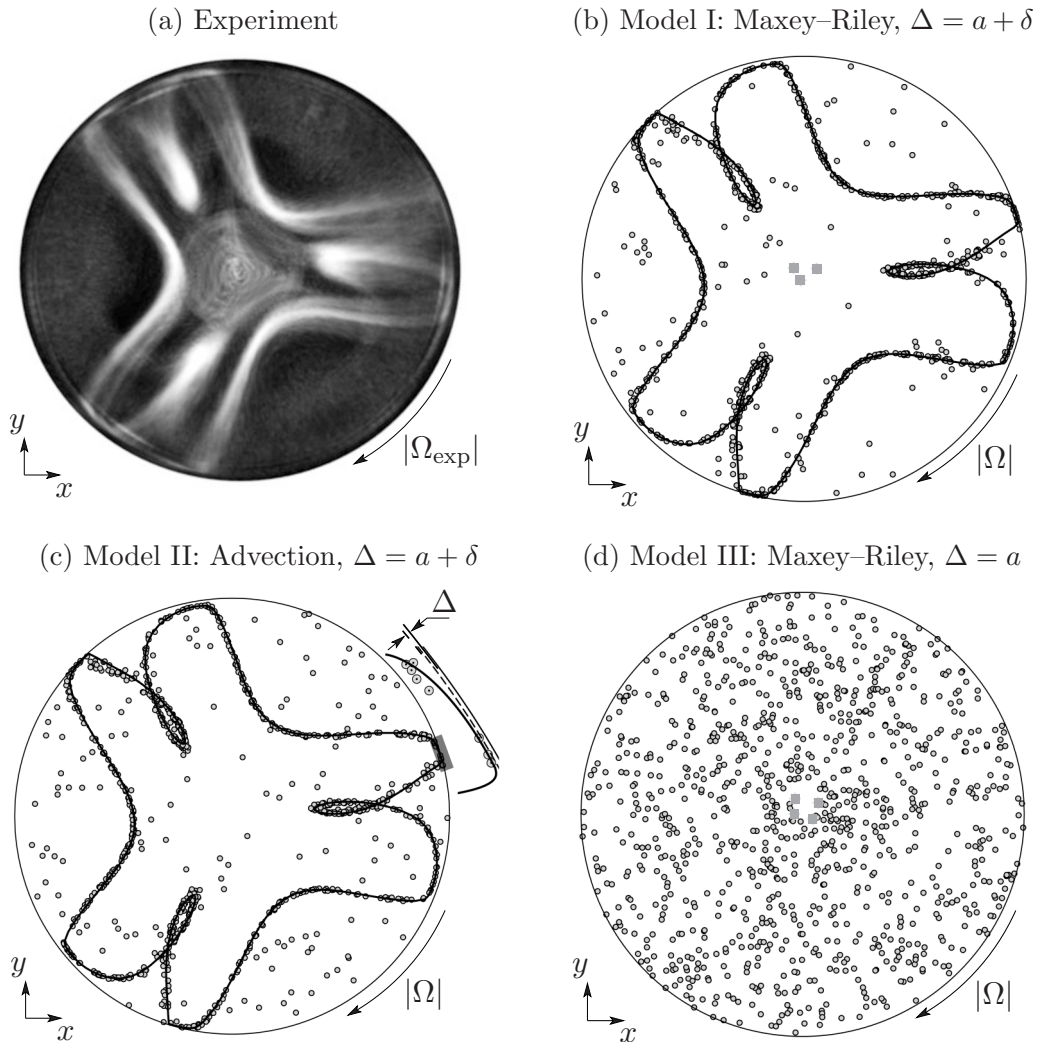


FIG. 10. Top view of finite-size Lagrangian coherent structures of SL-2 type for $\text{Re} = 1950$, $a = 0.002941$, and $\varrho = 2.52$ (corresponding to $\Delta = 0.00422$), shown in the rotating frame of reference. (a) Experimental result (courtesy I. Ueno, see Ref. [46]). [(b)–(d)] Particle configuration (light gray dots) at $t = 84$ resulting from numerical simulations according to model I (b), II (c), and III (d). The closed full line represents the closed streamline ${}^1L_3^6$ [see Fig. 8(d)]. In panel (c), also an enlargement is shown into the region near the free surface indicated by the dark gray rectangle. The arrow indicates the direction of propagation of the pattern in the laboratory frame. The light gray full squares denote immobile particles having settled on the cold bottom wall.

1. SL-2 PAS: The role of flow topology, inertia, and particle-surface interaction

To probe PAS, we consider $\text{Re} = 1950$ for which the so-called SL-2 PAS [11] is observed [Fig. 10(a)]. In the experiments, the SL-2 particle attractor is found only within a very narrow range of particle parameters. Therefore, only numerical simulations in which the particle scales are properly taken into account should be able to reproduce the experimental results. Here we use the same particle size and density as in the experiment of Ref. [39], i.e., particles with nondimensional radius $a = 0.002941$ and density ratio $\varrho = 2.52$. The Stokes and Froude numbers are $\text{St} = 4.844 \times 10^{-6}$ and $\text{Fr} = 9.11 \times 10^{-3}$, respectively.

For the numerical simulations, 1000 particles are initially randomly distributed in a subvolume of the domain $\mathcal{V}^* = (r, \varphi, z) \in [0, R^*] \times [0, 2\pi] \times [-1/2, 1/2]$, where $R^* = 1/\Gamma - \Delta$, and their trajectories are integrated up to $t = 84$ in units of the characteristic viscous diffusion time corresponding to three thermal diffusion times. This timescale is suggested by the experiments of Gotoda *et al.* [38], who found fully developed PAS after about approximately d^2/κ .

To clarify the relative importance of the different dissipation mechanisms, simulations are carried out for three different particle-motion models.

Model I: The Maxey-Riley equation (11) is integrated using the PSI model with $\Delta = a + \delta$, where δ is selected according to Romanò and Kuhlmann [21].

Model II: Particles are simply advected integrating (10) and using the PSI model with $\Delta = a + \delta$, where δ is selected according to Romanò and Kuhlmann [21].

Model III: The Maxey-Riley equation (11) is integrated using the PSI model, but neglecting the lubrication gap width δ by setting $\Delta = a$.

The experimental SL-2 particle accumulation pattern is shown in Fig. 10(a) in which many frames of a movie have been averaged in the rotating frame of reference [46]. Figures 10(b)–10(d) show the particle configurations obtained numerically at $t = 84$ employing models I, II, and III. Except for small details, model I [Fig. 10(b)] and model II [Fig. 10(c)] closely reproduce the experimental SL-2 PAS. In both cases, particles accumulate very near (or even on) the closed streamline ${}^1L_3^6$ of the KAM torus ${}^1T_3^6$ which is a pure property of the flow. Model III [Fig. 10(d)] fails to predict PAS. The following conclusions can be drawn from the comparison.

(a) Particle buoyancy is insignificant for the parameters of Fig. 10. Merely very few particles settle on the cold wall [gray squares near the center in Figs. 10(b) and 10(d)]. This is confirmed by neglecting particle buoyancy in model I: Corresponding simulations yield results (not shown) qualitatively identical to Figs. 10(b) and 10(c).

(b) Since the results obtained from models I and II are very similar and model II differs from model I by neglecting the inertia and buoyancy terms, it can be concluded that the inertial and buoyancy terms retained in the Maxey-Riley equation are not required to form SL-2 PAS. For the parameters of the experiment considered, PAS is correctly predicted when using the advection model (II) for the particle motion in the bulk.

(c) The comparison of model III [Fig. 10(d)] with model I [Fig. 10(b)] shows that neglecting the lubrication film thickness δ in the interaction parameter Δ leads to the fatally wrong result shown in Fig. 10(d). This underlines the importance of correctly selecting the interaction parameter Δ . The sensitivity of the accumulation pattern with respect to Δ can be understood in the framework of the PSI model [14]: Since the KAM tube within which particles accumulate (near the closed streamline) is very slender, particles moving in the region of the chaotic sea cannot be transferred to the regular KAM torus by the particle-surface interaction if the value for Δ is not correct. In that case, the PSI maps collided particles back to the chaotic sea. For a model flow, this is explained in detail by Muldoon and Kuhlmann [19] and for $\text{Pr} = 4$ by Mukin and Kuhlmann [18].

(d) If SL-2 PAS could form on the timescale considered solely due to inertia effects modeled by the Maxey-Riley equation, accumulation should have been visible in Fig. 10(d). Since this is not the case, with the particle distribution being nearly random at $t = 84$, it can be concluded that inertia effects are not the cause of SL-2 PAS in the experiment shown in Fig. 10(a). This conclusion refines conclusion (b) above.

From these considerations, it is deduced that SL-2 PAS in the experiment is exclusively due to the particle-surface interaction and that the interaction parameter must be selected correctly. This result is consistent with earlier results for the smaller Prandtl number $\text{Pr} = 4$ [14,18] in which inertia was neglected, and with the results of Muldoon and Kuhlmann [33]. These previous results, as well as the current investigation, show the physical mechanism leading to such Lagrangian coherent structures is based on the strong correlation between the flow topology and the interaction parameter Δ which depends on the particle size (radius a) and the lubrication gap width δ for the given flow conditions. The present simulations confirm the general mechanism of Hofmann and Kuhlmann [14] according

to which PAS (here SL-2 PAS) is caused by the transfer of particles moving in the chaotic sea to a regular region of the flow by means of particle-surface interactions (see also Refs. [18,19]).

For the system under investigation, the correction of the purely advective motion of particles by inertia effects modeled by (6) is small, which is also suggested by the small Stokes number $St = 4.844 \times 10^{-6}$. Therefore, when a particle moves in a chaotic region of the flow, its motion is quasiergodic and will tend to explore the chaotic sea without significantly being affected by its finite size. But when the particle moves close to the free surface, its finite size becomes relevant and the particle is repelled from the free surface. In the model framework, this interaction transfers the particle from a chaotic to a regular region of the flow if $\Delta \approx \Delta_{fs}$ and if the particle-surface interaction arises upstream of the region of closest approach to the free surface of the KAM torus (for details, see Refs. [14,18,19]). This first phase of particle accumulation is very rapid due to the chaotic mixing outside of the KAM tori. In the second phase, the trapped particles become focused due to repeated encounters with the interface. Theoretically, weak inertia renders closed streamlines attractive or repulsive with the inertia-induced limit cycle evolving from the closed streamline as St increases from zero [56]. However, before the inertia-induced limit cycle for small St can attract particles, these are caught by the limit cycle created by the particle-surface interaction. Both limit cycles are different, but both are located in the vicinity of the closed streamline.

Since the SL-2 limit cycle caused by the particle-surface interaction is located very near the closed streamline ${}^1L_3^6$, particles moving on the limit cycle remain sufficiently distant from the solid walls. If a particle-wall collision model is implemented by setting $\Delta = a$ or $\Delta = a + \delta$, the evolution of the particle distribution is essentially the same and leads to the same particle limit cycle. The reason is the number of particle-wall interactions is far less than 0.1% of the number of particle-free-surface interactions, since Δ_{fs} is always three to five times smaller than Δ_w (Table II). Therefore, particle-wall interactions mainly occur in the initial phase when particles are randomly distributed. In the final phase of PAS formation, particle-wall interactions do not occur. For this reason, the particle wall-interaction can be neglected for the parameters investigated. Note that particle attractors can be caused by particle-wall collisions alone if the particle-free-surface interaction is disregarded (see Fig. 9 of Melnikov and Shevtsova [36]). However, such a model is expected to yield unphysical results whenever $\Delta_{fs} < \Delta_w$, which is usually the case.

A second example of SL-2 PAS, now for $Re = 1850$, is shown in Figs. 11(a) and 11(b), where a comparison is made between the experimental and the numerical SL-2 PAS. The numerical result [Fig. 11(b)] is obtained for model II (advection and PSI model). The value for the interaction length $\Delta = 0.00497$ was taken from the fit proposed by Romanò and Kuhlmann [21] based on the experimental parameters [$\Delta_{exp} = \Delta(a_{exp}, \varrho_{exp})$]. As for $Re = 1950$, a good agreement between the experimental and numerical PAS is obtained for $Re = 1850$. Since the KAM torus ${}^1T_3^6$ has a very small cross section, an accurate estimate of Δ is, once again, fundamental to numerically find SL-2 PAS.

2. SL-1 PAS

It was shown that advection in the bulk combined with the PSI model (model II) very well captures the physics of PAS. Therefore, we shall consider model II in the following, neglecting the weak dissipation introduced by inertia and buoyancy.

For a given Reynolds number in the range $Re \in [1825, 1900]$, particles have been found to accumulate either on SL-1 PAS (${}^1T_3^3$) or on SL-2 PAS (${}^1T_3^6$) [11,39]. Which attractor is realized depends on the particle size and particle-to-fluid density ratio, which both influence the interaction length Δ . This experimental result is confirmed by the present simulations using model II. For $Re = 1850$, we find different attractors depending on the interaction parameter Δ . Apart from the SL-2 PAS for $Re = 1850$ discussed above, we also find linelike PAS of type SL-1 and tubular PAS of type SL-1. While tubular SL-2 PAS can arise in principle, it would hardly be distinguishable in experiments from linelike PAS, because the cross section of the largest KAM torus is very small.

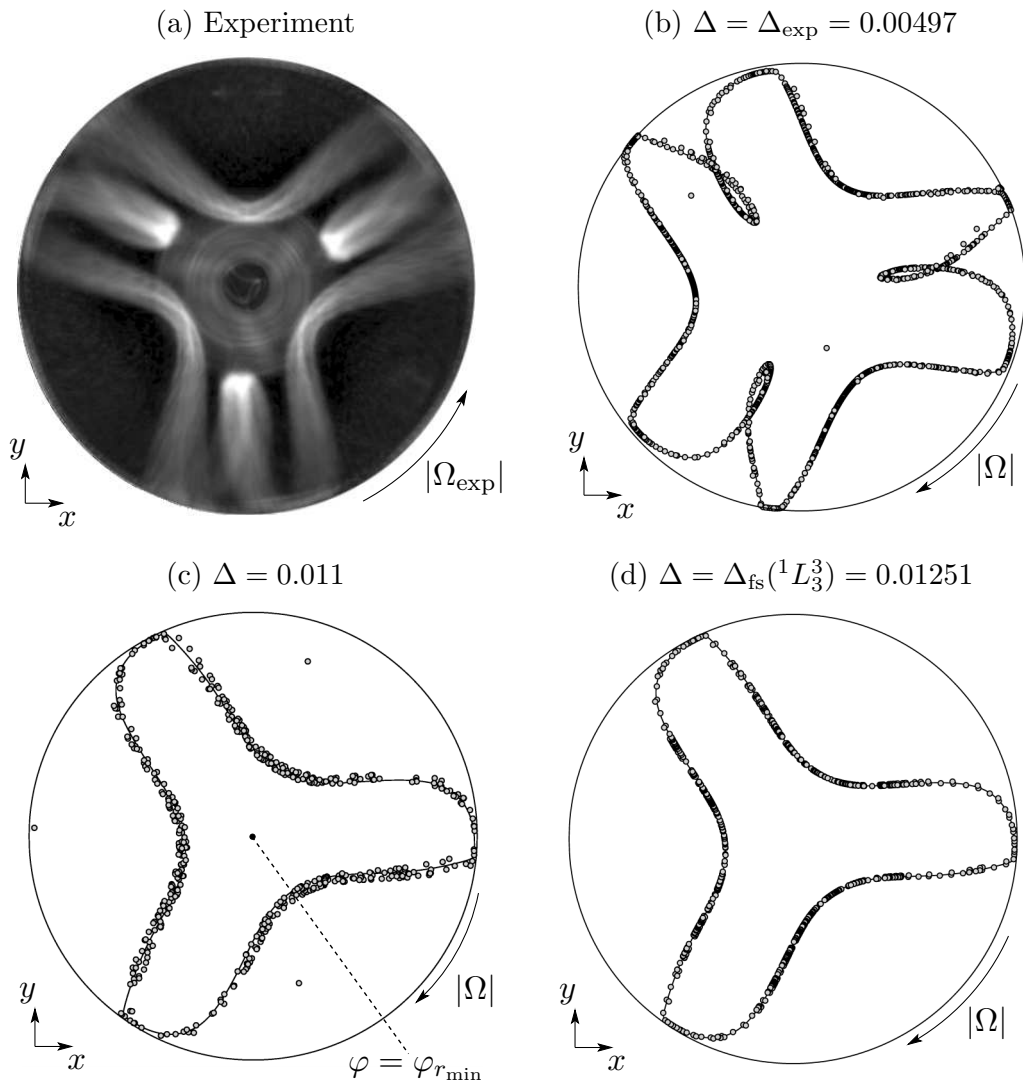


FIG. 11. Top view of finite-size Lagrangian coherent structures for $\text{Re} = 1850$ shown in the rotating frame of reference. (a) Experimental result for $a = 0.00424$, and $\varrho = 1.77$ (courtesy I. Ueno, see Ref. [46]). [(b)–(d)] Particle configuration (light gray dots) at $t = 50$ using the advection model II. Closed streamlines of the KAM tori ${}^1T_3^6$ (b) and ${}^1T_3^3$ [(c), (d)] from Fig. 8(c) are shown as full lines. The simulations differ by the interaction parameter: (b) $\Delta = \Delta_{\text{exp}} = 0.00497$, selected according to the experiment (line-like SL-2 PAS), (c) $\Delta = 0.011$ (tubular SL-1 PAS), and (d) $\Delta = \Delta_{\text{fs}}({}^1L_3^3) = 0.01251$ (line-like SL-1 PAS). The dashed line refers to one of the three azimuths at which the closed streamline admits its minimum radial coordinate: $\varphi = \varphi_{r_{\min}} = -0.9460$. The arrow indicates the direction of propagation in the laboratory frame. Using model I instead of model II yields visually indistinguishable particle attractors (not shown).

Linelike SL-1 PAS for $\text{Re} = 1850$ is shown in Fig. 11(d) for $\Delta = 0.01251 = \Delta_{\text{fs}}({}^1L_3^3)$. In this case, the closed streamline ${}^1L_3^3$ is tangent to the cylindrical surface $r = R^*$. The linelike PAS for purely advected particles coincides with the closed streamline under this tangency condition [14].

According to Hofmann and Kuhlmann [14], tubular PAS arises if $\Delta_{\text{fs}}({}^kT_i^j) < \Delta < \Delta_{\text{fs}}({}^kL_i^j)$. This is confirmed here, as we find tubular SL-1 PAS for $\text{Re} = 1850$ and interaction length

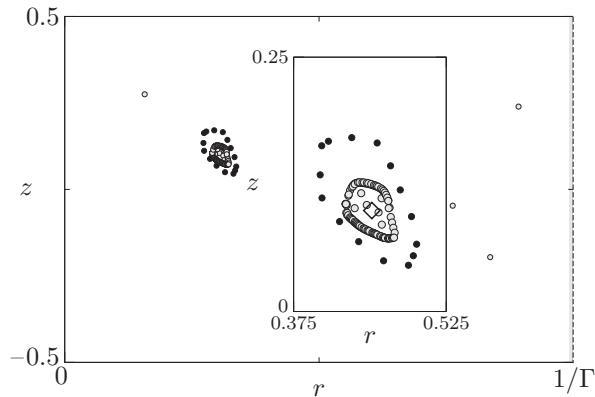


FIG. 12. Poincaré section at $\varphi = \varphi_{r_{\min}} = -0.9460$ of particle trajectories (gray dots) during the time interval $t \in [80, 84]$ for $\text{Re} = 1850$ and $\Delta = 0.011$ (tubular SL-1 PAS) corresponding to Fig. 11(c). The black dots delineate the largest reconstructible KAM torus ${}^1T_3^3$ and the diamond marks the closed streamline. The light gray strip at the right boundary indicates the prohibited region of width Δ inaccessible by the particle centroid within the PSI model. The inset shows an enlargement.

$\Delta = 0.011 \in [\Delta_{\text{fs}}({}^1T_3^3), \Delta_{\text{fs}}({}^1L_3^3)]$. The correlation of this tubular PAS with the KAM torus ${}^1T_3^3$ and ${}^1L_3^3$ is evident from Fig. 11(c), where the particles accumulate about the closed streamline. The tubular structure is better seen in the Poncaré section for $t \in [80, 84]$ shown in Fig. 12. The section is taken at the azimuth $\varphi = \varphi_{r_{\min}}$ at which the closed streamline ${}^1L_3^3$ attains its smallest radial coordinate $r_{\min}({}^1L_3^3)$. The particles form tubular SL-1 PAS about ${}^1L_3^3$, but are fully embedded in ${}^1T_3^3$. Most of particles accumulated on the KAM surface tangent to the cylinder $r = R^*$ [Fig. 12(b)]. A few Poincaré points are seen inside the tubular PAS. These result from particles initiated inside the KAM torus which do not experience any collisions and remain unaffected by the PSI model. All other particles initialized outside of the tubular attractor are transferred to the largest KAM surface which does not intersect with $r = R^*$, i.e., the tangent one, such that the particle motion on that torus does not experience any effective dissipation within the PSI model.

For $\text{Re} < 1825$ ($\text{Ma} \lesssim 51\,000$), only SL-1 PAS is reported [39]. This is confirmed by our numerical simulations, even though we find a new highly periodic PAS for $\text{Re} = 1600$ (see below) which may be difficult to distinguish in experiments from SL-1 PAS. The absence of SL-2 in the experiments (and simulations) underlines the key role of the KAM tori for PAS, because for Reynolds numbers $\text{Re} < 1825$ only a ${}^1T_3^3$ torus exists in the flow—the ${}^1T_3^6$ torus is absent [Figs. 8(a), 8(b) 9(a), and 9(b)]. For $\text{Re} > 1900$ ($\text{Ma} \gtrsim 53\,200$), on the other hand, only SL-2 PAS is experimentally reported [39]. This is fully consistent with the flow topology found [Figs. 8(d) and 9(d)] in which only ${}^1T_3^6$ exists with ${}^1T_3^3$ being absent for $\text{Re} > 1900$. Therefore, only an SL-2 attractor for the particle motion exist for the typical experimental particle parameters [interaction parameters Δ , see Figs. 10(a), 10(b) and 10(d)].

The orbit time $\tau = O(2\pi/\Omega)$ of the closed streamline ${}^1L_3^6$ in the rotating frame of reference is of the same order of magnitude as three periods of oscillation of the traveling wave (fundamental mode $m = 3$) corresponding to a full revolution in the laboratory frame. Therefore, a fluid element (a purely advected particle) on ${}^1L_3^6$ does not experience a sizable mean azimuthal drift in the laboratory frame. However, the orbit time of ${}^1L_3^3$ in the rotating frame is approximately half as large as the one for ${}^1L_3^6$. Hence, the mean azimuthal velocity of advected particles on ${}^1L_3^3$ in the laboratory frame of reference is $2\pi/\tau + \Omega$ ($\Omega < 0$) such that the particle on ${}^1L_3^3$ moves opposite to the wave with about the same mean angular velocity as the hydrothermal wave. This result is consistent the experimental result for slightly different parameters of Tanaka *et al.* [11] (their Fig. 13 for $\Gamma = 0.64$ and $\text{Ma} = 4.2 \times 10^4$).

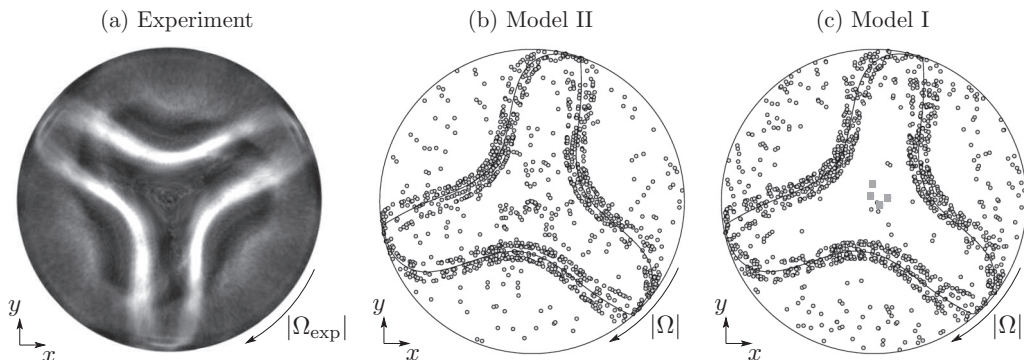


FIG. 13. (a) Experimental observation from the top view of the early phase of formation of SL-1 PAS for $Re = 1600$; $a = 0.00424$, $\varrho = 1.77$ (courtesy of I. Ueno, see Ref. [46]). The top view of the early phase of a numerically simulated SL-1 type of particle accumulation for $\Delta = 0.00552$ at $t = 25$ (1000 particles initially randomly distributed) is shown for model II (b) and model I (c). The closed streamline inside the ${}^1T_3^3$ torus is shown as a solid line. The particles are represented as light gray markers and the squares in panel (c) refer to settled particles.

3. Highly periodic tubular PAS

As the interaction parameter (particle size) is decreased from the tangent case tubular PAS will arise when the motion is advection dominated [14]. However, if $\Delta < \Delta_{fs}({}^kT_i^j)$ particles may be mapped back by the PSI to the chaotic region. Nevertheless, particle motion attractors can still exist in the chaotic sea (for an example, see Kuhlmann and Muldoon [57]).

Here we consider $Re = 1600$ and $\Delta = \Delta_{exp} = 0.00552 < \Delta_{fs}({}^1T_3^3) = 0.00565$ (Table II), motivated by experimental data for PAS shown in Fig. 13(a). Since the experimental image is not sharp the PAS may be interpreted as a usual SL-1 PAS. However, within our model tubular PAS of SL-1 (${}^1T_3^3$) does not exist any longer for such a small interaction parameter. We rather find another coherent structure for both models I and II. The early phase of this type of PAS is shown in Figs. 13(b) and 13(c) for $t = 25$. The final stage of PAS is depicted in Fig. 14 for $t = 84$, integrating 1000 particles initially randomly distributed using model II. We find that particles cluster on a structure which tightly wraps around the maximum reconstructible KAM torus ${}^1T_3^3$. On a first inspection [Figs. 14(a) and (b)], the accumulation structure appears as a line which closes on itself after five revolutions about the axis; therefore, $k = 5$ and $j = 15$. The azimuthal wave number is $m = 3$, slightly perturbed by the small-amplitude contaminations in the spectrum of the velocity field. The Poincaré section at $\varphi = \varphi_{r_{min}} = -1.7293$ during $t \in [80, 84]$ shown in Fig. 14(c) reveals that a closed streamline ${}^5L_3^{15}$ exists (diamond in the inset), surrounded by very thin KAM tori ${}^5T_3^{15}$ (black dots), which winds about the primary ${}^1T_3^3$ torus. This secondary structure, called resonance, is well known [58]. From Fig. 14(c), the particles form tubular PAS of type ${}^5T_3^{15}$ (gray dots) just outside of the KAM torus shown as black dots in the inset. Within our advection model, the tubular accumulation structure also marks the KAM torus of type ${}^5T_3^{15}$ which is tangent to $r = R^*$ for $\Delta = 0.00552$. This is consistent with $\Delta_{fs}({}^5T_3^{15}) = 0.00562$ and $\Delta_{fs}({}^5L_3^{15}) = 0.00582$.

Unfortunately, the experimental image [Fig. 13(a)] does not allow us to make a distinction between linelike SL-1 PAS of type ${}^1T_3^3$ and the present tubular PAS of type ${}^5T_3^{15}$ [Fig. 14(b)]. In this regard, a clarification would be of interest by, e.g., experimental Poincaré sections of long-time trajectories of individual particles.

The correlation between Eulerian and Lagrangian topological features is evident from Fig. 14(a) showing the isosurface $\theta = 0.5$ (light gray and transparent), the largest reconstructible KAM torus ${}^1T_3^3$ (dark gray), and particles forming tubular PAS of type ${}^5T_3^{15}$ (dark spheres), clearly outside of ${}^1T_3^3$. The correlation between the convection of temperature and the advection of particles has already

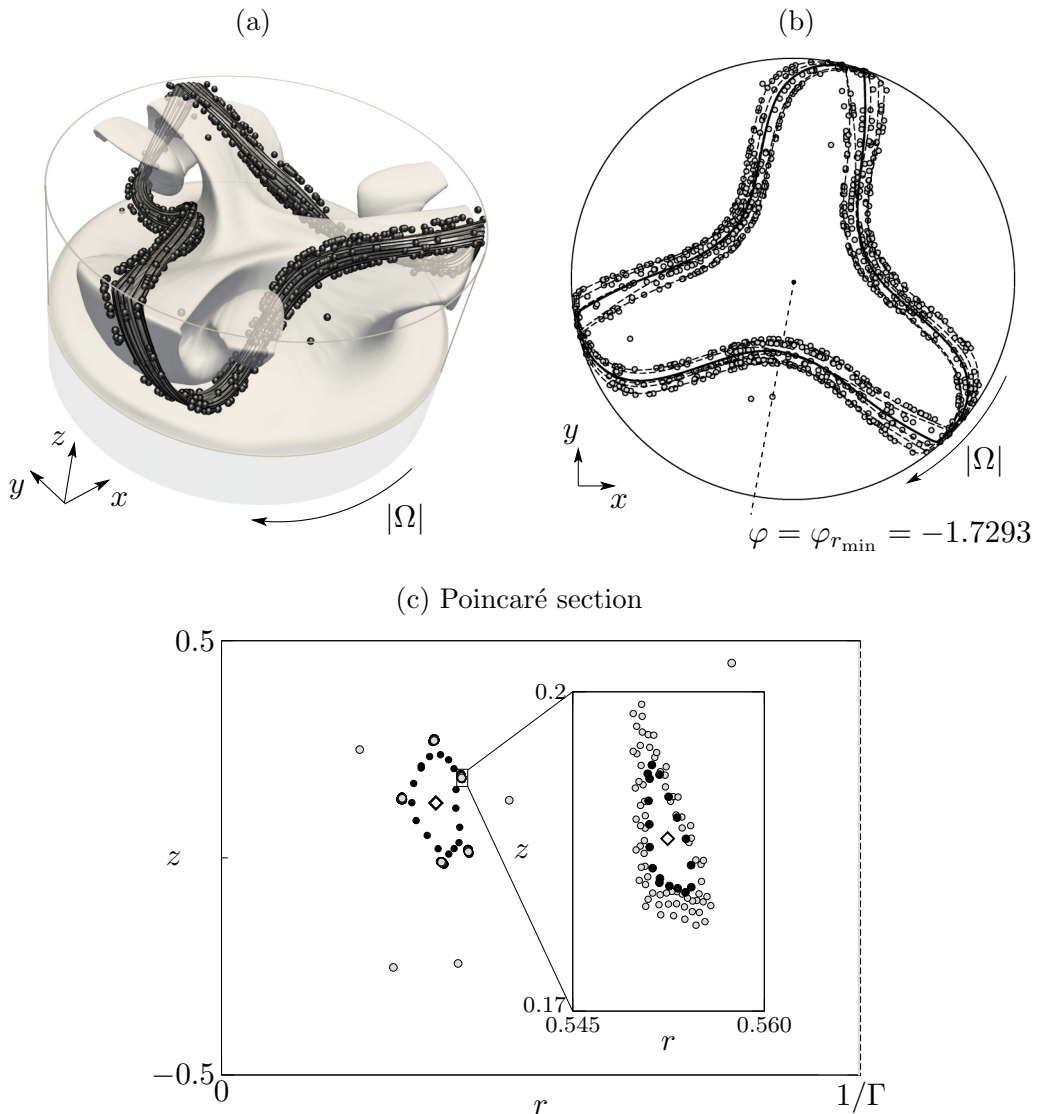


FIG. 14. Particle accumulation structure for $\text{Re} = 1600$ and $\Delta = \Delta_{\text{exp}} = 0.00552$ at $t = 84$ from an initially random distribution of 1000 particles using model II. (a) Three-dimensional view in the rotating frame showing the outermost KAM torus (dark gray), the temperature isosurface $\theta = 0.5$ (light gray transparent surface), and particles (dark spherical markers). (b) Axial projection of panel (a) without the temperature field. The solid line indicates ${}^1L_3^3$ and the dashed line denotes ${}^5L_3^{15}$. The arrow indicates the direction of propagation of the pattern in the laboratory frame. (c) Poincaré section (gray dots) at $\varphi = \varphi_{r_{\min}} = -1.7293$ during $t \in [80, 84]$ of the closed streamline ${}^1L_3^3$ (diamond) and of ${}^1T_3^3$ (black dots). The thin gray strip of thickness Δ adjacent to the free surface indicates the prohibited region for the particle centroids. The enlargement shows the Poincaré section of ${}^5L_3^{15}$ (diamond), ${}^5T_3^{15}$ (black dots), and PAS (gray dots).

been observed by Schwabe *et al.* [12] for fluids with Prandtl numbers in the range from 8 to 15. They found particles on PAS to approach the free surface closest in regions where the surface temperature has its local minima (cold surface spots). For $\text{Pr} = 28$ and SL-1 PAS, on the other hand, Toyama *et al.* [39] found the closest approach of the particles to the free surface to arise in a region between

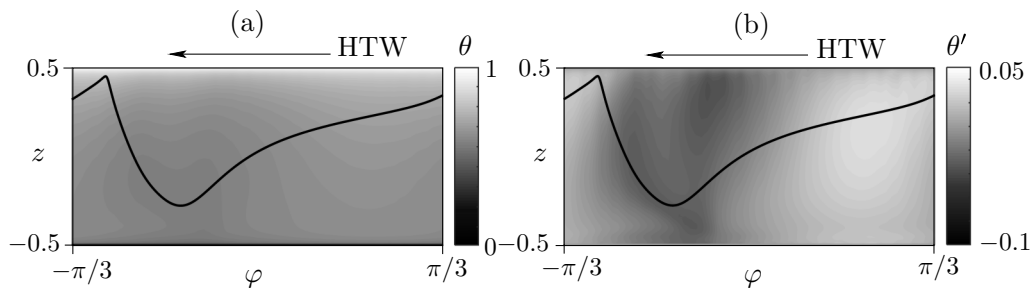


FIG. 15. Correlation between the free surface temperature θ (a) (grayscale), the free surface temperature deviation θ' (b) (grayscale), and the closed streamline ${}^1L_3^3$ in radial projection (solid line) for $\text{Re} = 1600$. The hydrothermal wave (HTW) wave travels from right to left (arrow).

the two surface temperature extrema (between the cold and the hot spot), even closer to the hot than to the cold spot. To clarify this discrepancy, we show in Fig. 15 the surface temperature (grayscale) together with the radial projection of the closed streamline ${}^1L_3^3$ (solid line) for $\text{Re} = 1600$. Shown in Fig. 15(a) is the surface temperature θ , while Fig. 15(b) shows the temperature deviation θ' from the azimuthal mean $\theta' = \theta - (2\pi)^{-1} \int_{-\pi}^{\pi} \theta d\varphi$. A particle on a limit cycle near ${}^1L_3^3$ would move near the full line from left to right in the figure. The sharp peak of ${}^1L_3^3$ indicates the beginning of the close approach to the free surface with the particle remaining close to it about halfway along the steep part of the projection of ${}^1L_3^3$. In agreement with Toyama *et al.* [39], the steep part of the closed streamline close to the interface is located just between the global maximum (bright) and the global minimum (dark) of the surface temperature fluctuation θ' [Fig. 15(b)]. As can be seen, the *global* minimum of the surface temperature fluctuation arises very close to the hot wall at about $\varphi = -0.241$, quite distant from the closest approach of ${}^1L_3^3$ to the free surface (steep part of the full line). The fluctuation of the free surface temperature distribution is caused by conduction from the bulk surface temperature and can be explained by the cold fingers [temperature isosurface shown in Figs. 5(a) and 14(a)]. On the first approach of a cold finger to the free surface, it leaves a weak cold spot on the free surface (*local* minimum of θ') just in the region where ${}^1L_3^3$ approaches the free surface closest [see Fig. 14(a)]. Upon the second return to the free surface of the cold finger, it leaves a second cold spot on the free surface (*global* minimum of θ'). This second surface spot is stronger than the first one, even though the cold finger has become weaker. However, since the cold finger approaches the free surface more closely during the second approach than during the first approach to the free surface, the stronger temperature conduction leads to the global minimum of θ' . We conclude that the closest approach of ${}^1L_3^3$ (and thus SL-1 PAS) to the free surface is associated with the cold surface temperature spot caused by the first approach of the cold finger to the free surface. For Prandtl numbers investigated by Schwabe *et al.* [12], this first cold spot is a global minimum of the free surface temperature fluctuation. For Prandtl number $\text{Pr} = 28$, however, due to the reduced thermal diffusion, the cold finger becomes much longer and approaches the free surface for a second time, leaving an even stronger cold spot which is not correlated with the closest approach of ${}^1L_3^3$ and SL-1 PAS to the free surface.

Apparently, the first (weak) cold spot associated with SL-1 PAS has not been detected in the experiments of Toyama *et al.* [39] in their Fig. 11 for $\text{Re} = 1679$. Possible reasons for the different surface temperature distributions obtained numerically by us and experimentally by Toyama *et al.* [39] may be related to (a) the Newton's cooling law and Biot number used to model the heat transfer across the free surface, (b) the free surface assumed cylindrical in our simulations, and/or (c) experimental errors committed in measuring the subtle details of the free surface temperature fluctuations. Nevertheless, the good agreement between numerical and experimental particle structures confirms advection in the bulk being the determining property for the bulk temperature and for PAS alike.

4. Toroidal core of particles

Another particle accumulation structure frequently observed together with the SL-1 and SL-2 shapes of PAS is the so-called *toroidal core of particles* (COP) [11,15]. The COP arises as a simple thick nonwinding toroidal structure of particles near the apparent vortex core of the basic flow.

Within the advection model (II) the COP arises, because the particle boundary interaction removes particles from streamlines which intersect with $r = R^*$. For hydrothermal waves, we always find a thin layer of chaotic streamlines just below the free surface. Therefore, particles are removed from those chaotic streamlines within the turnover time of the basic vortex flow such that the region near the z axis becomes rapidly depleted of particles [19,59]. The particles removed by the PSI are injected into the flow along the release line on $r = R^*$ (see Fig. 2) [14,18,19]. If a KAM torus exists which intersects with the release line, particles can be transferred to this KAM torus along the intersection, creating a periodic (linelike) or quasiperiodic (tubular) attractor.

The COP in the experiment shown in Fig. 13(a) has some fine structure. In previous numerical investigations of the topology of a model flow [19] and of the Navier-Stokes flow in liquid bridges with $\text{Pr} = 4$ [18], a nonwinding KAM torus was found to exist denoted T_{core} . Kuhlmann *et al.* [15] attributed the structures of the core found in experiments to other slender KAM tori (Fig. 7 of Mukin and Kuhlmann [18]) tightly winding about T_{core} which, like T_{core} , do not intersect with $r = R^*$ and thus can keep particles for a long time. For all cases investigated here ($\text{Pr} = 28$), we did not find a KAM torus representing T_{core} . However, the streamlines in the region of the vortex core are only weakly chaotic. This suggests that T_{core} may exist at lower Reynolds numbers.

For the conditions of Fig. 13 ($\Delta = 0.00552$) tubular PAS of type ${}^5T_3^{15}$ forms rapidly, while at the intermediate time $t = 25$ other particles are still moving in the core region [Fig. 13(b)]. This is even more evident using model I and disregarding particles settled on the cold wall [gray squares in Fig. 13(c)]. Since the flow in the core region is weakly chaotic, the COP is transient. On a longer timescale, it loses particles, by PSI, to the tubular ${}^5T_3^{15}$ PAS, which is a global attractor. This numerical observation suggests the COP seen in the experiment in Fig. 13(a) is transient as well.

In the presence of attractors due to KAM tori, the transient COP has vanished after three thermal diffusion times ($t = 84$) for the flows investigated. For particle parameters Δ for which no line- or tubelike KAM-induced attractor exists, the weakly chaotic COP can arise for even longer times. This is demonstrated in Fig. 16 considering $\text{Re} = 1750$ and $\Delta = 0.01, 0.02$, and 0.03 . For $\Delta = 0.01$, we find tubular PAS inside the KAM torus ${}^1T_3^3$ [Fig. 16(a)], because $\Delta \in [\Delta_{\text{fs}}({}^1T_3^3), \Delta_{\text{fs}}({}^1L_3^3)]$. Increasing the interaction parameter to $\Delta = 0.02$, beyond the minimum distance of the closed streamline from the free surface [$\Delta = 0.02 > \Delta_{\text{fs}}({}^1L_3^3) = 0.01462$], period doubling [18] of SL-1 PAS is found [Fig. 16(b)]. The period-doubled structure resides outside of the KAM torus ${}^1T_3^3$. Within model II, the particles move on chaotic streamlines and the fuzziness of the structure could indicate a chaotic attractor. A similar period doubling was also found in experiments [40]. Finally, for $\Delta = 0.03$ periodic and period-doubled attractors are absent and the particle structure at $t = 84$ can be interpreted as a COP [Fig. 16(c)]. This long-lived COP, however, is still transient. Since all particles are advected on weakly chaotic streamlines they will suffer repeated free-surface interactions. For long times, they thus move on the release surface, defined as the stream surface evolving forward in time from the union of all release points and subject to the PSI model [19]. At large time $t = 280$, we find all particles moving on the release surface to be attracted to a limit cycle shown in Figs. 16(d) and 16(e). Its period is $\tau = 1.652$ such that the particles in the laboratory frame of reference move with the mean angular velocity $2\pi/\tau + \Omega = -0.497$ in the same direction as the hydrothermal wave, similar to that observed by Tanaka *et al.* [11] for particles belonging to the COP. The limit cycle is made from segments of chaotic streamlines, connected by small trajectory segments on R^* along which the PSI is active [bold in Fig. 16(e)]. The nonsmooth character of the limit cycle (in the framework of the PSI model) is similar as for linelike PAS in the regular region of the flow when $\Delta > \Delta_{\text{fs}}(T)$.

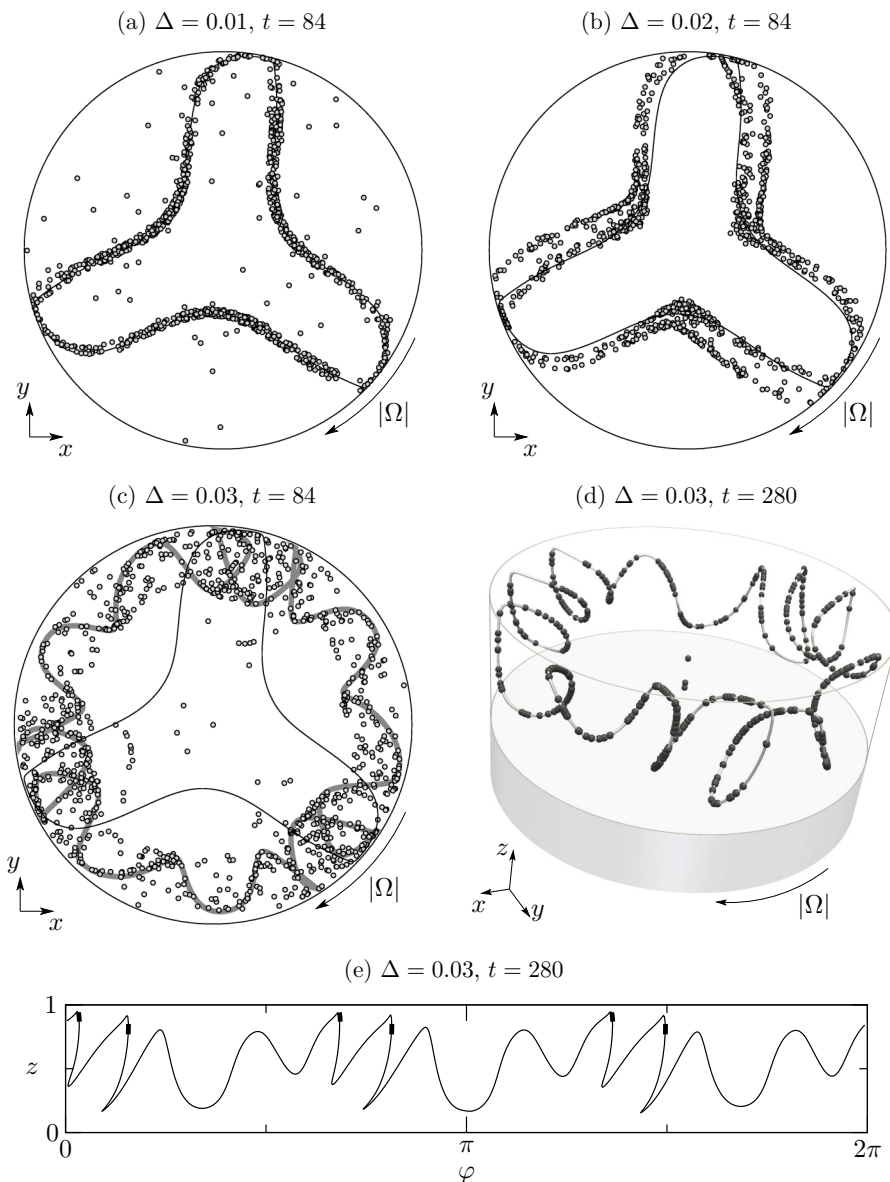


FIG. 16. PAS for $\text{Re} = 1750$ and $\Delta = 0.01$ (a), 0.02 (b), and 0.03 [(c)–(e)] using model II and 1000 initially randomly distributed particles. Shown at time $t = 84$ are tubular PAS for $\Delta = 0.01$ (a), fuzzy period-doubled PAS for $\Delta = 0.02$ (b), and the toroidal core for $\Delta = 0.03$ (c). Panel (d) shows a three-dimensional view of the particle configuration together with the attractor (line) at $t = 280$ and panel (e) shows the radial projection of the attractor. The bold segments in panel (e) indicate the PSI.

V. DISCUSSION AND CONCLUSIONS

The flow structure of traveling hydrothermal waves in a cylindrical thermocapillary liquid bridge and the motion of suspended particles has been computed for aspect ratio $\Gamma = 0.68$ and Prandtl number $\text{Pr} = 28$. The Reynolds and Grashof numbers were selected according to experimental conditions for which PAS has been reported. For conditions of the experiments with $\text{St} = \mathcal{O}(10^{-5})$

and a moderate density mismatch $\varrho = O(1)$, PAS can be accurately modeled using particle advection and the PSI model [14], provided the interaction length Δ is properly taken into account. The numerically computed PAS are in good agreement with the experimental results for SL-1 and SL-2.

By considering different particle motion models, it was shown that the dissipation necessary for the existence of an attractor in the dynamical system governing the particle motion in the experiments is due to the particle-surface interaction with particles essentially being advected in the bulk, as proposed by Hofmann and Kuhlmann [14] (PSI model). The PSI model considered is an example for a dynamical Filippov system [60] in which the dissipation originates solely from the normal-velocity discontinuity of the slip boundary at $r = R^*$ [61]. Since the particle repulsion from the free surface is caused by its finite size, the dissipative structure PAS is a *finite-size Lagrangian coherent structure*. It is not an *inertial Lagrangian coherent structure*, because inertia effects are insignificant for the cases considered.

As a key result, we find an extremely slender KAM torus in the rotating frame of reference with the shape of the well-known SL-2 type of PAS [11]. The KAM torus ${}^1T_3^6$ is a sole property of the flow. Its significance originates from material fluid elements being locked inside of the torus. This locking applies not only in the rotating frame of reference, where the KAM torus is stationary, but also in the laboratory frame of reference, because marking material elements is a scalar function. In the laboratory frame, the spiral nonmixing region ${}^1T_3^6$, as well as advected particles caught inside, are both wrapping about the basic vortex core such that the fluid and the PAS inside ${}^1T_3^6$ appear to rotate azimuthally. We also find SL-1 PAS to be associated with the somewhat thicker KAM torus ${}^1T_3^3$. Besides SL-1 and SL-2 types of PAS, a new and more subtle PAS was discovered which is associated with the very slender KAM torus ${}^5T_3^{15}$. The closed streamline ${}^5L_3^{15}$ winds 15 times about the vortex core and closes after five revolutions about the axis. Because of its fine structure ${}^5T_3^{15}$, PAS may easily be confused with ${}^1T_3^3$ PAS in experiments. These types of PAS are strictly related to KAM tori of the flow which, therefore, act as templates for PAS.

If we increase the Reynolds number, ${}^1T_3^3$ recedes from the free surface while remaining the same size up to $\text{Re} = 1750$. For $\text{Re} = 1850$, the cross section of ${}^1T_3^3$ is much smaller than for $\text{Re} = 1600$ (and $\text{Re} = 1750$); i.e., $\Delta_{\text{fs}}({}^1L_3^3) - \Delta_{\text{fs}}({}^1T_3^3)$ passes from ≈ 0.006 for $\text{Re} = 1600$ to ≈ 0.002 for $\text{Re} = 1850$. This strong decrease of the cross-sectional area of the KAM torus in a narrow range of Reynolds numbers explains why ${}^1T_3^3$ has not been found for $\text{Re} = 1950$. On the other hand, ${}^1T_3^6$ is found at $\text{Re} = 1850$. It seems to be a robust feature of the flow topology for moderately high Reynolds numbers and is preserved for $\text{Re} = 1950$. The KAM torus ${}^1T_3^6$ is characterized by a very small cross section and it is located closer to the free surface than ${}^1T_3^3$ ($\Delta_{\text{fs}}({}^1T_3^6) > \Delta_{\text{fs}}({}^1T_3^3)$).

For each KAM torus, there exists a specific window of particle parameters for which the accumulation is observed [11,33,36,39]. If the interaction length Δ is too small or too large, such that the particle-surface interaction cannot transfer the particles from the chaotic to the regular region of the flow, the typical linelike PAS is not observed [Fig. 10(d)]. When the KAM torus involved is very slender near the free surface, e.g., ${}^1T_3^6$ or ${}^5T_3^{15}$, the window of particle parameters for which the accumulation arises is very narrow. Under these conditions, an accurate estimate of the minimum lubrication gap between particle surface and the boundary [21] is mandatory to numerically reproduce the phenomenon.

When the interaction length Δ is increased, SL-1 and SL-2 linelike PAS cease to exist due to the incompatibility of the interaction parameter with the location of the KAM tori. Nevertheless, particles are repelled from the free surface and they can form accumulation structures outside of the KAM tori in the region of chaotic streamlines. One example for $\text{Re} = 1750$ is the linelike periodic PAS for $\Delta = 0.03$ which forms well inside the chaotic sea. On quite a long timescale, this PAS emerges from a transient core of particles in which particles move on weakly chaotic streamlines.

The advection and PSI model used represents the limit $\text{St} \rightarrow 0$ and a particle-surface interaction sharply localized at $r = R^*$. Since this limit is nonsingular, small deviations ($\text{St} \ll 1$, continuous PSI) will change the attractor continuously. This is confirmed by the good agreement with experiments in which the particle advection is slightly perturbed by inertial and buoyancy forces and in which the PSI is smooth. Therefore, model II is robust with respect to these small perturbations. The limitation

of the discontinuous PSI model mainly concerns the temporal evolution of PAS, which is expected to be slightly less rapid for a continuous PSI.

Gotoda *et al.* [38] and Toyama *et al.* [39] found the formation time for both SL-1 and of SL-2 PAS to be of the order of magnitude of the thermal diffusion time d^2/κ . It is clear that thermal diffusion is irrelevant for the particle motion and that Brownian motion can be neglected on the length and timescales of the particles used. However, the experiments are typically initiated from an undefined flow state and the subsequent evolution of the flow into a hydrothermal wave hosting PAS is influenced by the thermal diffusion, because the hydrothermal wave at large Pr is characterized by strong internal temperature extrema and a weak velocity field [9,62]. Therefore, the temporal evolution of PAS in the experiments is governed by different timescales: (a) The thermal diffusion timescale of the flow on which the fine KAM tori necessary for SL-1 and SL-2 PAS become steady in the rotating frame of reference, (b) the rate by which particles are transferred from the region of chaotic streamlines to the region of regular ones, and (c) the time required to focus the particles once they have entered the KAM torus [14]. It is *a priori* unclear which of the three processes is the limiting one. The present numerical evidence, however, suggests that the timescale on which particles are transferred from the chaotic to the regular region when the flow is fully developed is of the same order of magnitude as the thermal diffusion time.

These considerations indicate some open problems for future investigations, related to quantitative studies of particle inertia, particle buoyancy, particle-surface interaction, and the timescales of PAS formation. Another open problem relates to particle-particle interactions, which have been neglected here and which may become important during the final stage of PAS when the local particle density along the PAS becomes large.

ACKNOWLEDGMENTS

Support from Forschungsförderungsgesellschaft (FFG) under Project No. 840119 and from European Space Agency (ESA) through Contract No. 4000121111 is kindly acknowledged. We thank T. Lemée for preliminary computations and I. Ueno for images of PAS in experiments.

-
- [1] K. V. Sharp and R. J. Adrian, On flow-blocking particle structures in microtubes, *Microfluid. Nanofluid.* **1**, 376 (2005).
 - [2] R. M. Iverson, The physics of debris flows, *Rev. Geophys.* **35**, 245 (1997).
 - [3] S. Ida and D. N. Lin, Toward a deterministic model of planetary formation. I. A desert in the mass and semimajor axis distributions of extrasolar planets, *Astrophys. J.* **604**, 388 (2004).
 - [4] H. Burtscher, S. Künzel, and C. Hüglin, Characterization of particles in combustion engine exhaust, *J. Aerosol Sci.* **29**, 389 (1998).
 - [5] G. F. Paciotti, L. Myer, D. Weinreich, D. Goia, N. Pavel, R. E. McLaughlin, and L. Tamarkin, Colloidal gold: A novel nanoparticle vector for tumor directed drug delivery, *Drug Deliv.* **11**, 169 (2004).
 - [6] D. V. J. H. Mark and J. H. Vincent, A new personal sampler for airborne total dust in workplaces, *Ann. Occup. Hyg.* **30**, 89 (1986).
 - [7] H. C. Kuhlmann, *Thermocapillary Convection in Models of Crystal Growth* (Springer, Berlin, 1999).
 - [8] D. Schwabe, P. Hintz, and S. Frank, New features of thermocapillary convection in floating zones revealed by tracer particle accumulation structures (PAS), *Microgravity Sci. Technol.* **9**, 163 (1996).
 - [9] M. Wanschura, V. Shevtsova, H. C. Kuhlmann, and H. J. Rath, Convective instability mechanisms in thermocapillary liquid bridges, *Phys. Fluids* **7**, 912 (1995).
 - [10] M. Levenstam, G. Amberg, and C. Winkler, Instabilities of thermocapillary convection in a half-zone at intermediate Prandtl numbers, *Phys. Fluids* **13**, 807 (2001).
 - [11] S. Tanaka, H. Kawamura, I. Ueno, and D. Schwabe, Flow structure and dynamic particle accumulation in thermocapillary convection in a liquid bridge, *Phys. Fluids* **18**, 067103 (2006).
 - [12] D. Schwabe, A. I. Mizev, M. Udhayasankar, and S. Tanaka, Formation of dynamic particle accumulation structures in oscillatory thermocapillary flow in liquid bridges, *Phys. Fluids* **19**, 072102 (2007).

- [13] D. Schwabe, S. Tanaka, A. Mizev, and H. Kawamura, Particle accumulation structures in time-dependent thermocapillary flow in a liquid bridge under microgravity conditions, *Microgravity Sci. Technol.* **18**, 117 (2006).
- [14] E. Hofmann and H. C. Kuhlmann, Particle accumulation on periodic orbits by repeated free surface collisions, *Phys. Fluids* **23**, 072106 (2011).
- [15] H. C. Kuhlmann, R. V. Mukin, T. Sano, and I. Ueno, Structure and dynamics of particle-accumulation in thermocapillary liquid bridges, *Fluid Dyn. Res.* **46**, 041421 (2014).
- [16] H. Aref, Stirring by chaotic advection, *J. Fluid Mech.* **143**, 1 (1984).
- [17] J. M. Ottino, *The Kinematics of Mixing: Stretching, Chaos, and Transport* (Cambridge University Press, Cambridge, UK, 1989).
- [18] R. V. Mukin and H. C. Kuhlmann, Topology of hydrothermal waves in liquid bridges and dissipative structures of transported particles, *Phys. Rev. E* **88**, 053016 (2013).
- [19] F. H. Muldoon and H. C. Kuhlmann, Coherent particulate structures by boundary interaction of small particles in confined periodic flows, *Phys. D (Amsterdam, Neth.)* **253**, 40 (2013).
- [20] F. H. Muldoon and H. C. Kuhlmann, Numerical error in modeling of particle accumulation structures in periodic free-surface flows, *Comput. Fluids* **88**, 43 (2013).
- [21] F. Romanò and H. C. Kuhlmann, Particle-boundary interaction in a shear-driven cavity flow, *Theor. Comput. Fluid Dyn.* **31**, 427 (2017).
- [22] F. Romanò, H. C. Kuhlmann, M. Ishimura, and I. Ueno, Limit cycles for the motion of finite-size particles in axisymmetric thermocapillary flows in liquid bridges, *Phys. Fluids* **29**, 093303 (2017).
- [23] M. R. Maxey and J. J. Riley, Equation of motion for a small rigid sphere in a nonuniform flow, *Phys. Fluids* **26**, 883 (1983).
- [24] M. Orlishausen, L. Butzhammer, D. Schlotzbohm, D. Zapf, and W. Köhler, Particle accumulation and depletion in a microfluidic Marangoni flow, *Soft Matter* **13**, 7053 (2017).
- [25] D. O. Pushkin, D. E. Melnikov, and V. M. Shevtsova, Ordering of Small Particles in One-Dimensional Coherent Structures by Time-Periodic Flows, *Phys. Rev. Lett.* **106**, 234501 (2011).
- [26] D. E. Melnikov, D. O. Pushkin, and V. M. Shevtsova, Synchronization of finite-size particles by a traveling wave in a cylindrical flow, *Phys. Fluids* **25**, 092108 (2013).
- [27] H. C. Kuhlmann and F. H. Muldoon, Comment on “Ordering of Small Particles in One-Dimensional Coherent Structures by Time-Periodic Flows,” *Phys. Rev. Lett.* **108**, 249401 (2012).
- [28] H. C. Kuhlmann and F. H. Muldoon, Comment on “Synchronization of finite-size particles by a traveling wave in a cylindrical flow” [Phys. Fluids **25**, 092108 (2013)], *Phys. Fluids* **26**, 099101 (2014).
- [29] D. O. Pushkin, D. E. Melnikov, and V. M. Shevtsova, Pushkin, Melnikov, and Shevtsova Reply, *Phys. Rev. Lett.* **108**, 249402 (2012).
- [30] D. E. Melnikov, D. O. Pushkin, and V. M. Shevtsova, Response to “Comment on ‘Synchronization of finite-size particles by a traveling wave in a cylindrical flow’” [Phys. Fluids **26**, 099101 (2014)], *Phys. Fluids* **26**, 099102 (2014).
- [31] M. Lappa, Assessment of the role of axial vorticity in the formation of particle accumulation structures in supercritical Marangoni and hybrid thermocapillary-rotation-driven flows, *Phys. Fluids* **25**, 012101 (2013).
- [32] M. Lappa, On the variety of particle accumulation structures under the effect of g -jitters, *J. Fluid Mech.* **726**, 160 (2013).
- [33] F. H. Muldoon and H. C. Kuhlmann, Origin of particle accumulation structures in liquid bridges: Particle-boundary interactions versus inertia, *Phys. Fluids* **28**, 073305 (2016).
- [34] D. E. Melnikov, T. Watanabe, T. Matsugase, I. Ueno, and V. Shevtsova, Experimental study on formation of particle accumulation structures by a thermocapillary flow in a deformable liquid column, *Microgravity Sci. Technol.* **26**, 365 (2014).
- [35] M. Gotoda, D. E. Melnikov, I. Ueno, and V. Shevtsova, Experimental study on dynamics of coherent structures formed by inertial solid particles in three-dimensional periodic flows, *Chaos* **26**, 073106 (2016).
- [36] D. E. Melnikov and V. Shevtsova, Different types of Lagrangian coherent structures formed by solid particles in three-dimensional time-periodic flows, *Eur. Phys. J.: Spec. Top.* **226**, 1239 (2017).
- [37] Y. Abe, I. Ueno, and H. Kawamura, Effect of shape of HZ liquid bridge on particle accumulation structure (PAS), *Microgravity Sci. Technol.* **19**, 84 (2007).

- [38] M. Gotoda, T. Sano, T. Kaneko, and I. Ueno, Evaluation of existence region and formation time of particle accumulation structure (PAS) in half-zone liquid bridge, *Eur. Phys. J.: Spec. Top.* **224**, 299 (2015).
- [39] A. Toyama, M. Gotoda, T. Kaneko, and I. Ueno, Existence conditions and formation process of second type of spiral loop particle accumulation structure (SL-2 PAS) in half-zone liquid bridge, *Microgravity Sci. Technol.* **29**, 263 (2017).
- [40] M. Gotoda, A. Toyama, M. Ishimura, T. Sano, M. Suzuki, T. Kaneko, and I. Ueno, Experimental study on dynamics of finite-size particles in coherent structures induced by thermocapillary effect in deformable liquid bridge, *Phys. Rev. Fluids* (unpublished).
- [41] I. Ueno, S. Tanaka, and H. Kawamura, Oscillatory and chaotic thermocapillary convection in a half-zone liquid bridge, *Phys. Fluids* **15**, 408 (2003).
- [42] Y. Abe, I. Ueno, and H. Kawamura, Dynamic particle accumulation structure due to thermocapillary effect in noncylindrical half-zone liquid bridge, *Ann. NY Acad. Sci.* **1161**, 240 (2009).
- [43] A. Babiano, J. H. E. Cartwright, O. Piro, and A. Provenzale, Dynamics of a Small Neutrally Buoyant Sphere in a Fluid and Targeting in Hamiltonian Systems, *Phys. Rev. Lett.* **84**, 5764 (2000).
- [44] F. Romanò and H. C. Kuhlmann, Numerical investigation of the interaction of a finite-size particle with a tangentially moving boundary, *Int. J. Heat Fluid Flow* **62**, 75 (2016).
- [45] H. Brenner, The slow motion of a sphere through a viscous fluid towards a plane surface, *Chem. Eng. Sci.* **16**, 242 (1961).
- [46] H. C. Kuhlmann and T. Lemée, Particle accumulation in the JEREMI Experiment: Definition of necessary flow and particle parameters (PARTAC), FFG Report (ASAP) No. 840119, 2016 (unpublished).
- [47] J. R. Dormand and P. J. Prince, A family of embedded Runge-Kutta formulas, *J. Comput. Appl. Math.* **6**, 19 (1980).
- [48] M. Lappa, R. Savino, and R. Monti, Influence of buoyancy forces on Marangoni flow instabilities in liquid bridges, *Int. J. Num. Meth. Heat Fluid Flow* **10**, 721 (2000).
- [49] H. Kawamura and I. Ueno, Review on thermocapillary convection in a half-zone liquid bridge with high Pr fluid: Onset of oscillatory convection, transition of flow regimes, and particle accumulation structure, in *Surface Tension-Driven Flows and Applications*, edited by R. Savino (Research Signpost, 2006), pp. 1–24.
- [50] V. M. Shevtsova, D. E. Melnikov, and J. C. Legros, Multistability of oscillatory thermocapillary convection in a liquid bridge, *Phys. Rev. E* **68**, 066311 (2003).
- [51] I. Ueno (private communication).
- [52] F. Romanò, S. Albensoeder, and H. C. Kuhlmann, Topology of three-dimensional steady cellular flow in a two-sided anti-parallel lid-driven cavity, *J. Fluid Mech.* **826**, 302 (2017).
- [53] F. Romanò, A. Hajisharifi, and H. C. Kuhlmann, Cellular flow in a partially filled rotating drum: Regular and chaotic advection, *J. Fluid Mech.* **825**, 631 (2017).
- [54] K. Bajer, Hamiltonian formulation of the equations of streamlines in three-dimensional steady flow, *Chaos Solitons Fractals* **4**, 895 (1994).
- [55] H. G. Schuster, *Deterministic Chaos: An Introduction* (Wiley-VCH, Berlin, 2005).
- [56] H. C. Kuhlmann and F. H. Muldoon, Particle-accumulation structures in periodic free-surface flows: Inertia versus surface collisions, *Phys. Rev. E* **85**, 046310 (2012).
- [57] H. C. Kuhlmann and F. H. Muldoon, On the different manifestations of particle accumulation structures (PAS) in thermocapillary flows, *Eur. Phys. J.: Spec. Top.* **219**, 59 (2013).
- [58] A. J. Lichtenberg and M. A. Lieberman, *Regular and Stochastic Motion*, Applied Mathematical Sciences Vol. 38 (Springer Science+Business Media, New York, 1983).
- [59] H. C. Kuhlmann and T. Lemée, Particle-depletion dynamics in axisymmetric thermocapillary flows, *Eur. Phys. J.: Spec. Top.* **224**, 309 (2015).
- [60] A. F. Filippov, *Differential Equations with Discontinuous Righthand Sides: Control Systems* (Springer Science & Business Media, Berlin, 2013).
- [61] W. M. Haddad and T. Sadikhov, Dissipative differential inclusions, set-valued energy storage and supply rate maps, and stability of discontinuous feedback systems, *Nonlinear Anal. Hybri.* **8**, 83 (2013).
- [62] J. Leyboldt, H. C. Kuhlmann, and H. J. Rath, Three-dimensional numerical simulation of thermocapillary flows in cylindrical liquid bridges, *J. Fluid Mech.* **414**, 285 (2000).